Original Article

CAMBRIDGE
UNIVERSITY PRESS

The onset of Neo-Tethys subduction in the Early Jurassic: evidence from the eclogites of the North Shahrekord Metamorphic Complex (Sanandaj-Sirjan Zone, W Iran)

Chiara Montemagni[1] , Stefano Zanchetta[1], Nadia Malaspina[1], Hamid Reza Javadi[2] and Andrea Zanchi[1]

[1]Department of Earth and Environmental Sciences, University of Milano - Bicocca, Milan, 20126, Italy and [2]Geological Survey of Iran, Meraj Boulevard Tehran, Iran

Abstract

Geodynamic models implying subduction of continental crust either consider this process happening during collision, when the continental margin of the lower plate attempts subduction, or in pre-collisional stages, when tectonic erosion of the upper plate or subduction of continental extensional allochthons drag continental crust in the subduction channel. In the Zagros orogen (W Iran), high-pressure rocks are known only from the Sanandaj-Sirjan Zone, NE of the Main Zagros Thrust. Here, eclogites of the North Shahrekord Metamorphic Complex suggest subduction of continental crust slices derived from the upper plate (Central Iran) during the onset of the Neo-Tethys subduction along the southern margin of Iran. Eclogites record a clockwise pressure-temperature-time path, with pre-eclogitic epidote-amphibolites-facies phase assemblages preserved in garnet cores, a high-pressure stage, and a subsequent retrogression at amphibolite-facies conditions. By means of forward thermodynamic modelling and 40Ar/39Ar geochronology, the peak metamorphism has been constrained at 1.9-2.1 GPa and 550-600 °C, in the 191-194 Ma time span. The following retrogression during exhumation lasted at least until 144 Ma. Our data suggest that the onset of the Neo-Tethys subduction traces back prior to 190 Ma, involving together with the Neo-Tethys oceanic lithosphere also slices of the upper plate continental crust scraped off by means of tectonic erosion processes.

1. Introduction

High-Pressure (HP) metamorphic rocks are key to understand subduction-related processes (e.g. Agard *et al.* 2009; Cheng *et al.* 2015; Di Vincenzo *et al.* 2016). Eclogites can form at different times during the subduction-collision history (e.g. Spalla *et al.* 1996), from pre-collisional stages to final continent-continent collision, when continental crust of the lower plate can be subducted even at ultrahigh-pressure (UHP) conditions (e.g. Jolivet *et al.* 2003), thus providing invaluable information on the processes acting at mantle depths during the evolution of orogenic belts. Useful information on the tectonometamorphic evolution of eclogite-bearing units comes through the application of meso- and microstructural analyses, conventional geothermobarometry and forward thermodynamic modelling. Geochronological data add time constraints, framing the P-T evolution of high-pressure tectonometamorphic units in the whole geodynamic process that controls the birth and the evolution of an orogen.
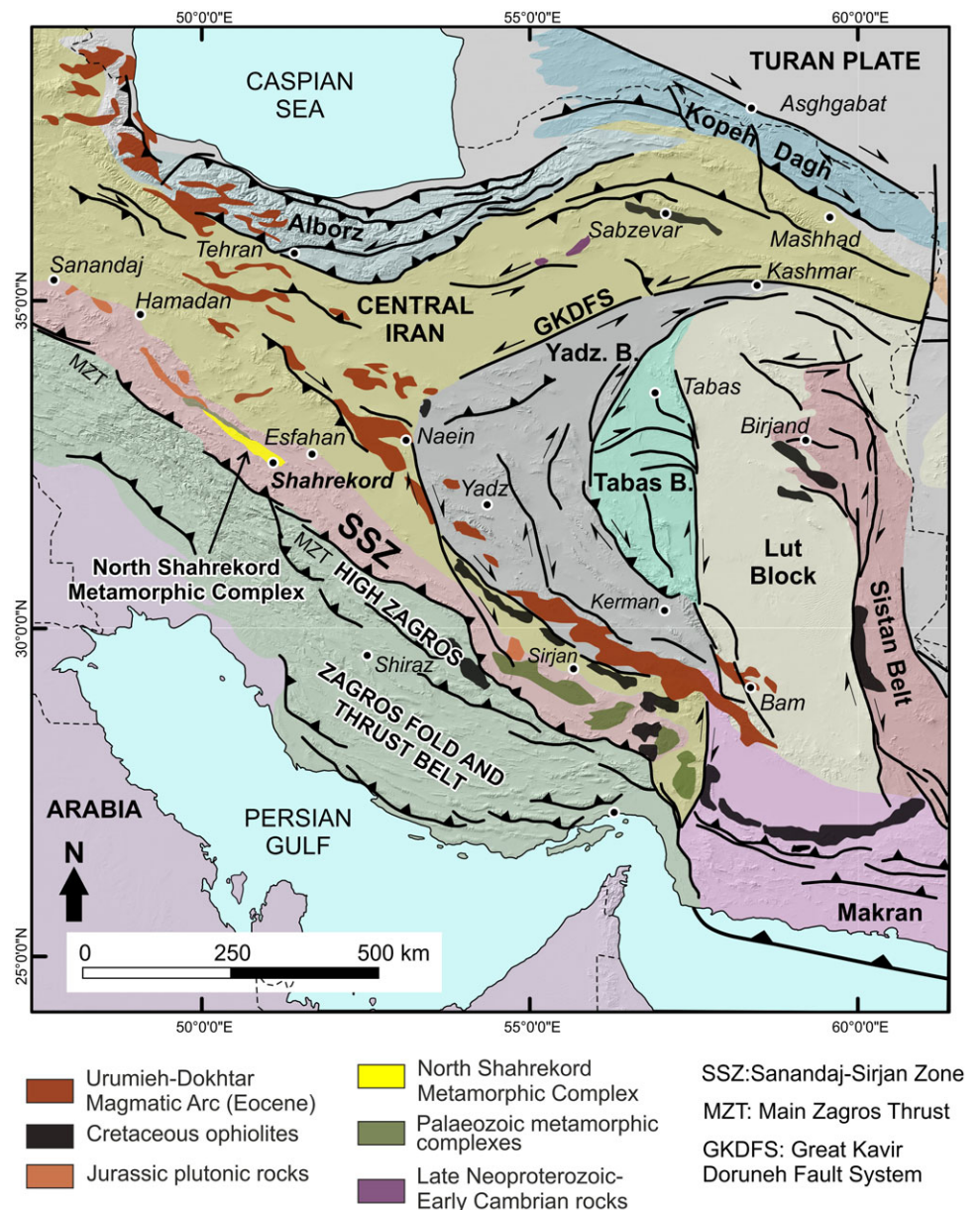
The 40Ar/39Ar method is one of the most used dating techniques when facing metamorphic rocks because it well constrains their thermal history and exhumation information (Di Vincenzo & Palmeri, 2001; Warren *et al.* 2012). Given their stability at HP and ultra (U)HP conditions, amphiboles and phengitic white micas are usually ideal minerals for 40Ar/39Ar dating.

The reconstructed P-T-t paths of continental HP rocks help to decipher the geodynamic scenario in which they formed, with special regard to their pre- or syn-collisional origin. Eclogites derived from continental crust may form at the end of the subduction of the intervening oceanic lithosphere between two continents, when slices of the continental crust of the lower plate are subducted below crustal depths. When derived from the upper plate, they can also form at the beginning or during the subduction in response to tectonic erosion processes (e.g. Polino *et al.* 1990; Massonne, 2012) that scrape off slices of the upper plate continental crust and drag them down along the subduction channel (e.g. Clift & Vannucchi, 2004; Vannucchi *et al.* 2008).

Here we present a multi-disciplinary study on the eclogites of the North Shahrekord Metamorphic Complex (NSMC, Sanandaj-Sirjan Zone, western Iran, Figure 1). The aim of this study is to unravel their Pressure-Temperature-time (P-T-t) path, providing information on the peak P-T conditions and their metamorphic evolution. The timing of the HP metamorphism

Figure 1. (Colour online) Tectonic scheme of Iran and surrounding areas. Modified after Zanchi *et al.* (2021). The location of the North Shahrekord Metamorphic Complex (NSMC) is highlighted.

and subsequent exhumation has been constrained by means of $^{40}Ar/^{39}Ar$ geochronology on eclogites and amphibolites, their retrogressed counterparts. Reconstructing the evolution of the NSMC eclogites is a key step in the understanding of the geodynamic processes associated with the onset and later stages of the Neo-Tethys subduction in western Iran.

Our results provide new P-T-t constraints on the onset and duration of eclogite facies metamorphism and subsequent amphibolite-facies retrogression in the Sanandaj-Sirjan Zone (Figure 1). Furthermore, the new data presented here, together with previously published petrological, geochemical and geochronological data on eclogites- and amphibolite-facies rocks (e.g. Davoudian *et al.* 2008, 2016; Malek-Mahmoudi *et al.* 2017; Jamali Ashtiani *et al.* 2020; Maghdour-Mashhour *et al.* 2021; Wan *et al.* 2023), refine the geodynamic model for the evolution of the Sanandaj-Sirjan Zone in western Iran. We propose here a new scenario involving the subduction of continental crust induced by the tectonic erosion of the overriding plate.

2. Geological background

The Alpine–Himalayan orogenic belt resulted from the closure of the Neo-Tethys Ocean and consequent continental collision between the Eurasian and the African–Arabian–Indian plates. In the central part of the Neo-Tethys, the collision between Eurasia and Arabia and several continental microplates (i.e. the Cimmerian blocks) caused the formation of the Turkish-Iranian plateau and of the associated orogenic belts during the Mesozoic-Cenozoic (Brunet & Cloetingh, 2003). The long-lasting convergence between the Eurasian and Arabian plates promoted the formation of the Zagros orogen (Agard *et al.* 2011), which consists of several NW-SE trending tectonic units. These tectonic units from NE to SW are as follows: (i) the Urumieh–Dokhtar Magmatic Arc, an arc mainly composed of Cenozoic plutonic and volcanic rocks (Schröder, 1944; Förster, 1974; Berberian & King, 1981; Berberian *et al.* 1982; Alavi, 1994); (ii) the Sanandaj–Sirjan Zone (SSZ, see Figure 1 in Stöcklin, 1968), representing a partially independent magmatic and metamorphic belt exposed to the NE of

the Zagros orogen (Agard *et al.* 2005; Mohajjel & Fergusson, 2014; Azizi *et al.* 2015a, 2015b; Moghadam *et al.* 2015; Shakerardakani *et al.* 2015; Hassanzadeh & Wernicke, 2016); (iii) the High Zagros consisting of imbricated tectonic slices of Mesozoic limestones, radiolarites and remnants of obducted ophiolites (Agard *et al.* 2005); (iv) the Zagros Fold-and-Thrust Belt; and (v) the Mesopotamian-Persian Gulf foreland basin (Berberian & King, 1981; Alavi, 1994; Mohajjel & Fergusson, 2000). The Main Zagros Thrust (MZT) is identified as the suture zone between the Arabian plate and the Cimmerian blocks, with the SSZ that developed in the upper plate during the subduction of the Neo-Tethys Ocean.

The SSZ is located along the southwestern edge of the Iranian plateau (Figure 1), running parallel to the Zagros orogen for about 1500 km from eastern Anatolia to the north-western Makran area (McCall, 2002). The SSZ consists of late Neoproterozoic and Pan-African basement (Crawford, 1977; Hassanzadeh *et al.* 2008; Nutman *et al.* 2014) that discontinuously crops out beneath Palaeozoic to Neogene metamorphic, igneous and sedimentary units (Agard *et al.* 2011; Jamshidi Badr *et al.* 2013; Mohajjel *et al.* 2003; Mohajjel & Fergusson, 2014; Moghadam *et al.* 2015; Shakerardakani *et al.* 2015; Sheikholeslami, 2015). The Palaeozoic sedimentary and magmatic record (Alirezaei & Hassanzadeh, 2012; Moghadam *et al.* 2015) of the SSZ is related to the opening of the Neo-Tethys that was in turn related to the rifting of continental fragments (i.e. the Cimmerian block, Ricou, 1994; Stampfli & Borel, 2002; Şengör & Yilmaz, 1981; Şengör, 1984; Zanchi *et al.* 2015) away from the northern margin of Gondwana during the Permian (Alavi, 1994; Angiolini *et al.* 2013, 2015; Agard *et al.* 2011; Hassanzadeh & Wernicke, 2016; Mattei *et al.* 2015; Moghadam *et al.* 2015; Zanchi *et al.* 2009a). During the Cimmerian orogeny (Late Triassic), these crustal blocks collided with the Eurasian plate following the closure of the Palaeo-Tethys (e.g. Wilmsen *et al.* 2009; Zanchi *et al.* 2009a; Zanchetta *et al.* 2013a; Zanchi *et al.* 2016). Even if the evolution of the Cimmerian blocks after their collision is still not completely resolved (Zanchi *et al.* 2009b; Zanchi *et al.* 2021 and references therein), their northern margin runs along the Palaeo-Tethys suture in north Iran and extends to northern Afghanistan, Pakistan, Pamir, Tibet and China (Angiolini *et al.* 2013, 2015; Zanchetta *et al.* 2018), and their southern boundary lies along the Neo-Tethys suture, namely the Main Zagros Thrust (MZT).

The switch from a passive continental margin to a continental arc in the SSZ occurred after the Cimmerian orogenic event, during the Late Triassic-Early Jurassic (Hassanzadeh & Wernicke, 2016; Maghdour-Mashhour *et al.* 2021), when the Neo-Tethyan NNE-NE-dipping subduction likely started. The Mesozoic to Cenozoic convergence finally led to the collision between the Arabian and the Eurasian plates (Mohajjel *et al.* 2003; Agard *et al.* 2005; Ghasemi & Talbot, 2006; Moritz *et al.* 2006). From the onset of the Neo-Tethys subduction to the collision with Arabia, the SSZ was not only affected by subduction-related magmatism but also by deformative and metamorphic events, mainly of Jurassic age (e.g. Fergusson *et al.* 2016), recorded in the several metamorphic-magmatic complexes scattered all along the SSZ (Jamshidi Badr *et al.* 2013), the most of them showing greenschist to amphibolite and even eclogite facies conditions (Mohajjel & Fergusson, 2000; Sheikholeslami *et al.* 2008; Ghasemi & Poor Kermani, 2009; Davoudian *et al.* 2016). Following Sheikholeslami (2015), the Jurassic rocks of the SSZ have been affected by, at least, two syn-metamorphic regional deformation phases: the first occurring in the Early Jurassic includes four deformation events; the second one resulted in three deformation events affecting Lower Jurassic

turbidites. During the first deformation phase, the metamorphic peak was reached at c. 187-180 Ma (U-Pb dating on Zrn; Fazlnia, 2007), whereas the HT peak metamorphism during the second deformational phase was constrained at c. 162 Ma (Sadegh *et al.* 2020).

The study area is located in the central SSZ in the North Shahrekord Metamorphic Complex (NSMC) west of Esfahan, belonging to the complexly deformed sub-zone (Figures 1 and 2). Here rare eclogite bodies occur as lenses or small-sized boudins within ortho- and paragneisses derived from the Gondwanan Pan-African basement of Iran (Davoudi *et al.* 2008, 2016; Nutman *et al.* 2014). The Gondwanan origin of the SSZ metamorphic belt has been proven (Fergusson *et al.* 2016) based on zircon ages pertaining to the Pan-African basement, which is exposed in wide areas of Central and Northwestern Iran (e.g. Hassanzadeh *et al.* 2008; Rahmati-Ilkhchi *et al.* 2011). U-Pb zircon ages also confirmed the Pan-African palaeogeographic affinity of granitic and metamorphic rocks near Golpaygan and around Lake Urumieh in the north-western sector of the SSZ (Fergusson *et al.* 2016 with references). Pan-African basement ages have been also documented in the central and northern Iranian Cimmerian continental blocks (Fergusson *et al.* 2016).

Eclogites of the NSMC occur as metre- to decametre-sized boudins hosted in amphibolites and paragneisses. Other units forming the NSMC consist of low- to very low-grade rocks such as schist, phyllite, marble, slate and metamorphosed sandstone, limestone, shale and volcanic rocks, with a possible Triassic to Jurassic age of the protoliths (U-Pb dating on Zrn; Davoudian *et al.* 2006; Babaahmadi *et al.* 2012).

3. Methods

3.a. Electron microprobe analyses

Electron microprobe analyses (EMPA) were carried out using a JEOL 8200 Super Probe EMP at the Department of Earth Sciences 'A. Desio', University of Milano. WDS (wavelength dispersive spectroscopy) quantitative chemical analyses and WDS X-ray elemental maps were performed on carbon-coated petrographic thin sections. Data acquisition was performed using an accelerating voltage of 15 kV, a beam current of 5 nA with a spot size of 3 μm on micas and 1 μm on other minerals. Oxides and natural silicates were used as standards. Analyses were recalculated to atom per formula unit (a.p.f.u.) as follows: garnet analyses were recalculated based on 8 cations and 24 charges; white mica was recalculated based on 11 oxygens and considering all Fe as Fe^{2+}; clinopyroxene data were elaborated following the procedure by Cawthorn & Collerson (1974) based on 12 oxygens and considering Fe^{3+} as the acmite component; amphiboles analyses were recalculated based on 23 oxygens and 13 cations plus K, Na, Ca. Amphibole data were classified and plotted according to Hawthorne & Oberti (2007).

3.b. $^{40}Ar/^{39}Ar$ geochronology

Samples selected for $^{40}Ar/^{39}Ar$ dating were crushed and sieved in order to separate white mica (in the fraction 250-500 μm) and amphibole (in the fraction 125-250 μm) for stepwise heating experiments. The separates were enriched in white mica and amphibole using a Frantz magnetic separator and handpicked under a stereomicroscope. Mineral separates were then cleaned ultrasonically in deionised water and wrapped in aluminium foil. Samples and standards were irradiated for 30 MWh in a fast neutron flux at the McMaster University Research Reactor (Hamilton, CA).
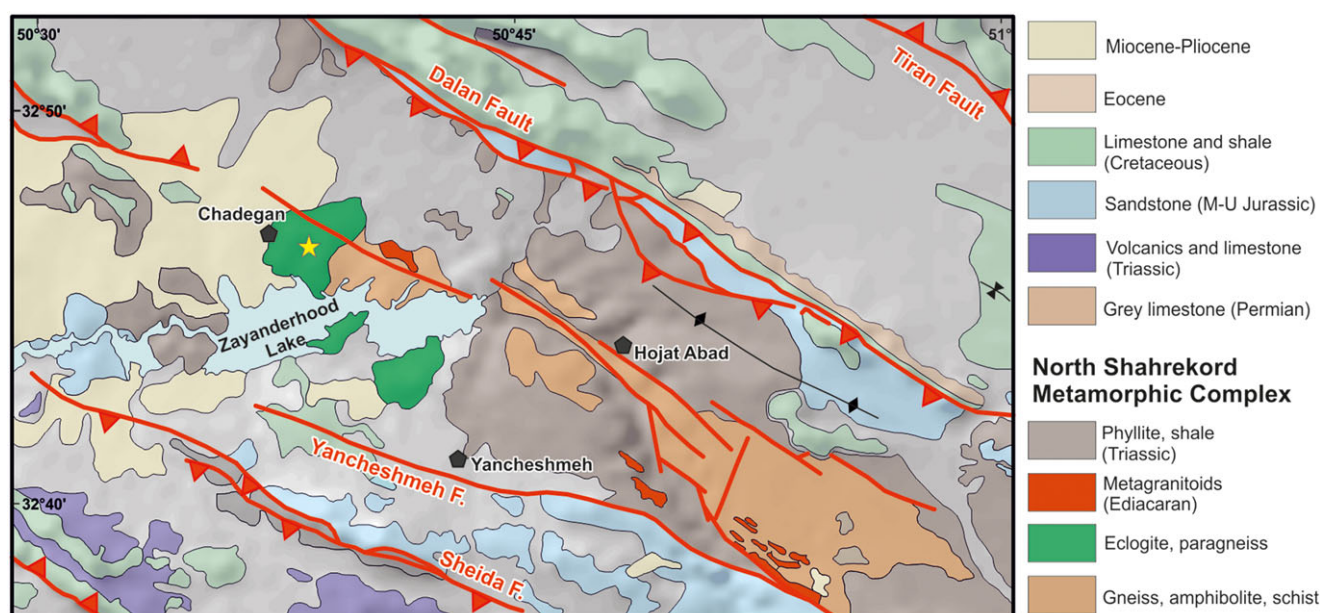
Figure 2. (Colour online) Simplified geological map of the NSMC in the Zayanderhood Lake area according to our field surveys and after Davoudian et al. (2016). The intrusion age of the metagranitoid has been constrained to be Ediacaran (Jamali Ashtiani et al. 2020). The yellow star shows the location of Chadegan eclogites analysed in this study.

Stepwise heating experiments were performed at the 'Laboratorio di Geocronologia' of the University of Milano–Bicocca following the procedure reported in Montemagni & Villa (2021) and Montemagni & Zanchetta (2022). Sample and standards were loaded in a double vacuum resistance furnace attached to a NuInstruments™ Noblesse® noble gas mass spectrometer, equipped with one Faraday collector with a $1011\,\Omega$ resistor and two MasCom™ ion counters. The samples were heated in 10 steps for 20 min each at temperatures from 620 °C to 1300 °C. The irradiation intensity factor, J, was interpolated for each sample from the equation defined by the J values of the monitors. The ^{40}K decay constant used for the age calculation was $5.543 \times 10^{-4}\,Ma^{-1}$ (Steiger & Jäger, 1977). To control the vertical flux gradient, monitors of McClure Mountain hornblende (MMhb) were interlayered with the sample disk wraps. The MMhb age was assumed to be 523.98 ± 0.12 Ma (Schoene & Bowring, 2006). Data reduction procedures, corrected for mass spectrometer background, ion counter gains, blank measurements, source fractionation and decay of ^{37}Ar since irradiation, were processed in the in-house CalcolAr Excel spreadsheet, in which also all the associated uncertainties are propagated.

3.c. Thermodynamic modelling

Thermodynamic modelling in the SiO_2 (46.71 wt%), Al_2O_3 (15.37 wt%), FeO (10.25 wt%), MgO (8.30 wt%), CaO (10.47 wt%), Na_2O (2.97 wt%), K_2O (0.87), TiO_2 (1.41 wt%), MnO (0.18 wt%), H_2O + CO_2 (1.80 wt%, LOI in Table 1) compositional system (sample Z5S in Table 1) was performed with the software package Perple_X 7.1.5 (http://www.perplex.ethz.ch; Connolly, 2005), using the thermodynamic database of Holland & Powell (2011) (hp62ver.dat). The whole rock major elements composition was determined on the best-preserved eclogite (sample Z5S) by ICP-MS analysis at the ACME analytical laboratories (Vancouver, Canada) by Inductively Coupled Plasma Emission Spectrometry (ICP-ES) for major and minor elements and Inductively Coupled Plasma Mass Spectrometry (ICP-MS) for trace elements, including the rare earth elements, after fusion with lithium metaborate/tetraborate and

digestion by diluted HNO_3. Loss on ignition (LOI) was determined by weight difference after ignition at 1000 °C. Blank analyses were always below the minimum detection limit for each element, and the analytical protocol included the analysis of the reference materials (standards) OREAS184, SO-19, OREAS30A and OREAS262.

We used the following solution models: Gt(W), Chl(W) and Ctd(W) for garnet, chlorite and chloritoid from White et al. (2014), Omph(GHP) for clinopyroxene from Green et al. (2007), CAmph(G) for amphibole from Green et al. (2016), Pheng(HP) for white mica from Holland & Powell (1998), Sp(WPC) for spinel after White et al. (2002), feldspar from Fuhrman & Lindsley (1988) and cCcM(EF) for carbonate from Franzolin et al. (2011). The H_2O-CO_2 (CORK) equation of state was taken from Holland & Powell (1998). Considering the low vol% amount of epidote (only in small inclusions in garnet) and of aegirine component in clinopyroxene, for the sake of simplicity, we considered the total iron in the bulk as Fe^{2+}.

4. Field occurrence and relationships

The NSMC (North Shahrekord Metamorphic Complex) consists of three main tectonometamorphic units (Davoudian et al. 2016): an eclogite-bearing unit located in the area of the Zayandeh-Rood Lake, a low-grade unit extending SE of the lake, mainly made of phyllites (Figure 2), and a third unit, mainly consisting of gneisses, amphibolites and schists, cropping out to the east in a tectonic window within the low-grade metamorphic unit. Lenses of weakly deformed metagranitoids of Ediacaran intrusion age (U-Pb on Zrn, Jamali Ashtiani et al. 2020) occur in the two units.

The contacts between the eclogite-bearing unit and surrounding ones are hardly visible due to poor exposures (Figure 3a). Amphibolites of the third unit frequently show a (proto)mylonitic fabric, suggesting that they are in contact with the rocks of the HP unit through a ductile shear zone. Eclogites occur as metre-sized to several decametre-sized boudins within country rocks (Figure 3c), which mainly consist of garnet-bearing paragneiss and granitoid

Table 1. Whole rock analyses of eclogites. Major elements are expressed as oxide wt%, trace elements as ppm

Sample	Z3S	Z4S	Z5S	Z7S
SiO_2	45.77	48.41	46.71	46.82
TiO_2	1.16	1.56	1.41	1.39
Al_2O_3	17.09	14.68	15.37	15.04
Fe_2O_3	10.37	12.56	11.39	11.89
MgO	9.01	7.29	8.30	8.11
CaO	11.25	10.87	10.47	10.55
Na_2O	2.09	2.61	2.97	2.76
K_2O	0.60	0.53	0.87	0.83
P_2O_5	0.09	0.13	0.14	0.09
MnO	0.16	0.20	0.18	0.18
Cr_2O_3	0.051	0.025	0.058	0.048
LOI	2.1	0.8	1.8	1.7
Sc	35	44	41	39
V	234	306	277	298
Cr	349	171	397	328
Co	48.6	44.2	43.4	42.1
Ni	135	45	90	48
Ga	16.0	17.3	16.6	15.6
Rb	15.2	20.6	20.6	19.8
Sr	211.9	246.8	184.4	201.5
Y	21.9	31.2	27.4	28.3
Zr	73.3	107.1	97.1	103.4
Nb	4.2	6.2	6.4	6.1
Ba	389	865	148	354
Cs	0.1	0.4	0.1	0.1
La	6.2	7.5	8.0	7.7
Ce	13.6	17.8	18.0	18.1
Pr	1.94	2.63	2.56	2.66
Nd	8.9	12.6	12.5	12.4
Sm	2.78	3.82	3.62	3.73
Eu	1.03	1.47	1.22	1.31
Gd	3.66	5.12	4.61	5.07
Tb	0.61	0.82	0.74	0.78
Dy	3.90	5.49	4.84	4.98
Ho	0.82	1.17	1.04	1.12
Er	2.34	3.29	3.04	3.12
Tm	0.37	0.48	0.42	0.41
Yb	2.23	2.98	2.74	2.78
Lu	0.34	0.46	0.41	0.42
Hf	2.1	3.1	2.4	2.6
Th	0.5	0.7	0.8	0.6
U	0.2	0.2	0.2	0.2

(Continued)

Table 1. (Continued)

Sample	Z3S	Z4S	Z5S	Z7S
Ta	0.3	0.4	0.4	0.3
ΣREE	48.72	65.63	63.74	64.58
ΣLREE	33.42	44.35	44.68	44.59
ΣHREE	14.27	19.81	17.84	18.68
Eu/Eu*	0.99	1.02	0.91	0.92
(La/Yb)n	1.994	1.805	2.094	1.987
(La/Sm)n	1.440	1.267	1.427	1.333
(Gd/Yb)n	1.358	1.421	1.392	1.509

Note: LOI: Loss On Ignition; n subscript – normalization to chondrite values (McDonough & Sun, 1995); ΣLREE – light rare earth element sum; ΣHREE – heavy rare earth elements sum; Eu/Eu* = Eun/RADQ(Smn × Gdn).

orthogneiss (Figure 3d and 3e). The regional foliation in paragneiss and orthogneiss dips to S-SSW at low to medium angle (Figure 3). Detailed structural relationships within the eclogite-bearing unit of the NSMC are not available since the strong weathering and the dispersed occurrence of outcrops (Figure 3a) significantly hamper their reconstruction in the field. However, where observable, the eclogitic boudins are always hosted in garnet paragneiss (Figure 3c).

Eclogites display different degrees of retrogression, ranging from almost fresh eclogites with the HP mineral phase assemblage still well preserved, to garnet and epidote amphibolites. Retrogression of the eclogitic lenses is coupled with an increase in deformation, with former boudins that are progressively stretched along the main foliation of the hosting paragneisses (Figure 3b). Eclogitic lenses display a foliation and/or compositional layering developed at small angle with respect to the paragneiss foliation that wraps around the boudins. The mineralogical layering is defined by alternating omphacite-phengite rich and garnet-amphibole rich levels, with the shape preferred orientation of omphacite, phengite and clinozoisite that marks the foliation.

5. Metamorphic evolution of the NSMC eclogites

Petrographic observations were performed on all lithologies of the metamorphic complex. Representative microstructures of the main equilibrium phase assemblages are reported in Figure 4. Mineral abbreviations are after Whitney & Evans (2010) except for white mica (Wm).

Our study was focussed both on fresh or only partially retrogressed eclogite samples (Figure 4a-f), in order to reconstruct the evolution of the equilibrium phase assemblages and to define the P-T evolution of the eclogite-bearing unit of the NSMC. The degree of retrogression after the HP stage is variable from eclogites still almost completely preserving the HP phase assemblage (Figure 4a-b), to eclogites completely retrogressed into epidote amphibolites.

Two-mica orthogneiss (Figure 4g) and garnet-bearing paragneiss (Figure 4h) are also found in the NSMC, either showing a foliation made by micas enveloping feldspar (Figure 4g) or garnet (Figure 4h) porphyroblasts. Most of the orthogneisses were garnet-bearing, as testified by the occurrence of abundant chlorite pseudomorphs after garnet porphyroblasts (Figure 4g).
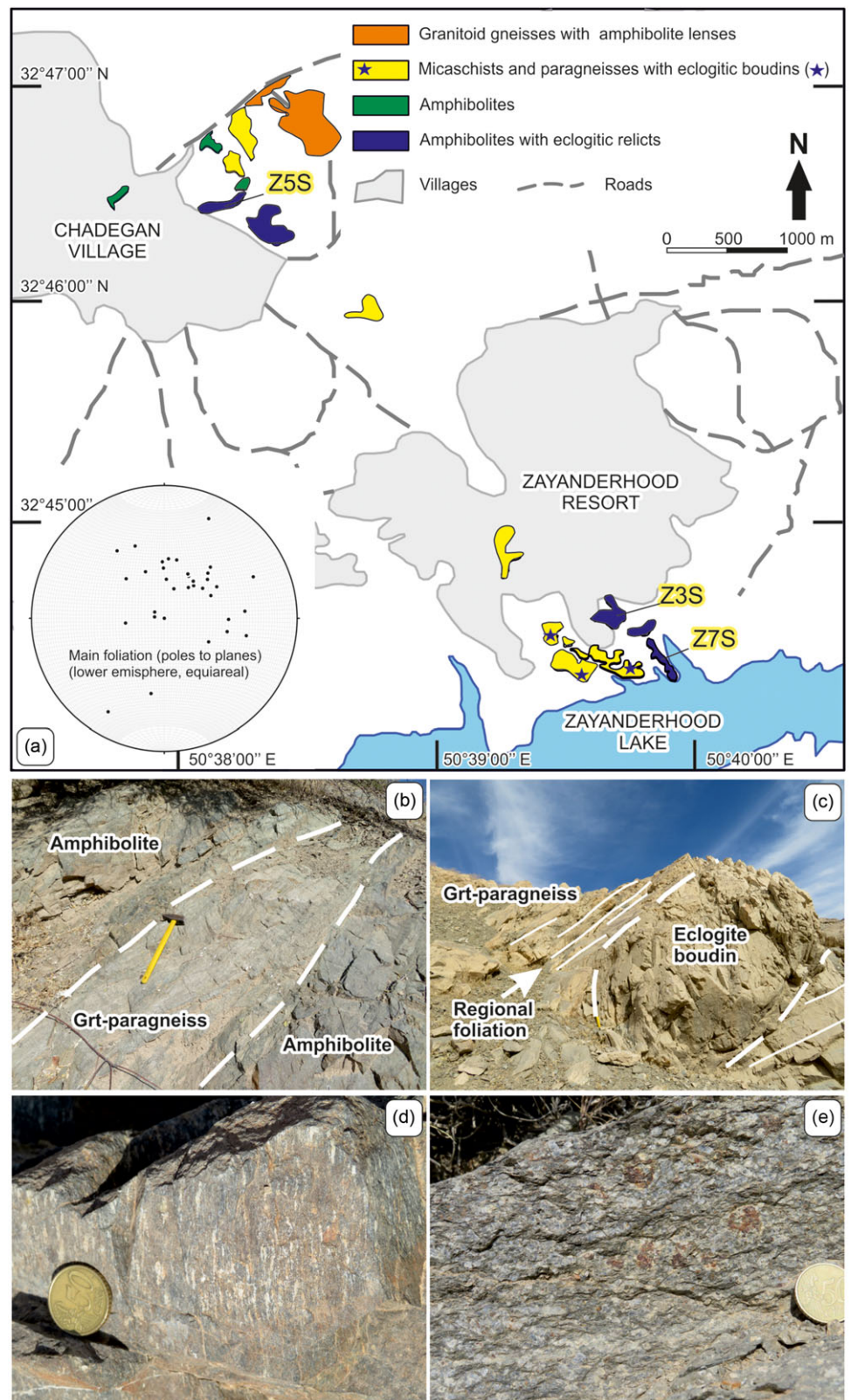
Figure 3. (Colour online) (a) Outcrops map of the NSMC rocks in the Chadegan area according to our field surveys. The location of the analysed samples has been reported. Field aspect of eclogites and surrounding rocks: (b) amphibolite layers stretched along the main foliation of the hosting paragneisses; (c) eclogitic boudins hosted in garnet paragneiss. The regional foliation in paragneiss has been highlighted. (d) Eclogite texture as appearing in the field, with a marked foliation and weakly developed compositional layering; (e) Grt-bearing granitoid orthogneisses.

The preserved eclogites (Figure 4a) are made of omphacite, garnet, white mica, clinozoisite, amphibole, epidote, plagioclase and quartz; rutile and ilmenite are the main accessory phases, whereas apatite and zircon are rare. Calcite also occurs in some samples, in lath-shaped crystals parallel to the omphacite foliation.

Based on petrographic and microstructural observations, three equilibrium phase assemblages, and relative metamorphic stages, can be reconstructed and summarized as follows (Figure 5):

(1) pre-eclogite facies preserved as inclusions within garnet cores (stage I in Figure 5); (2) a HP eclogite facies stage (stage II in
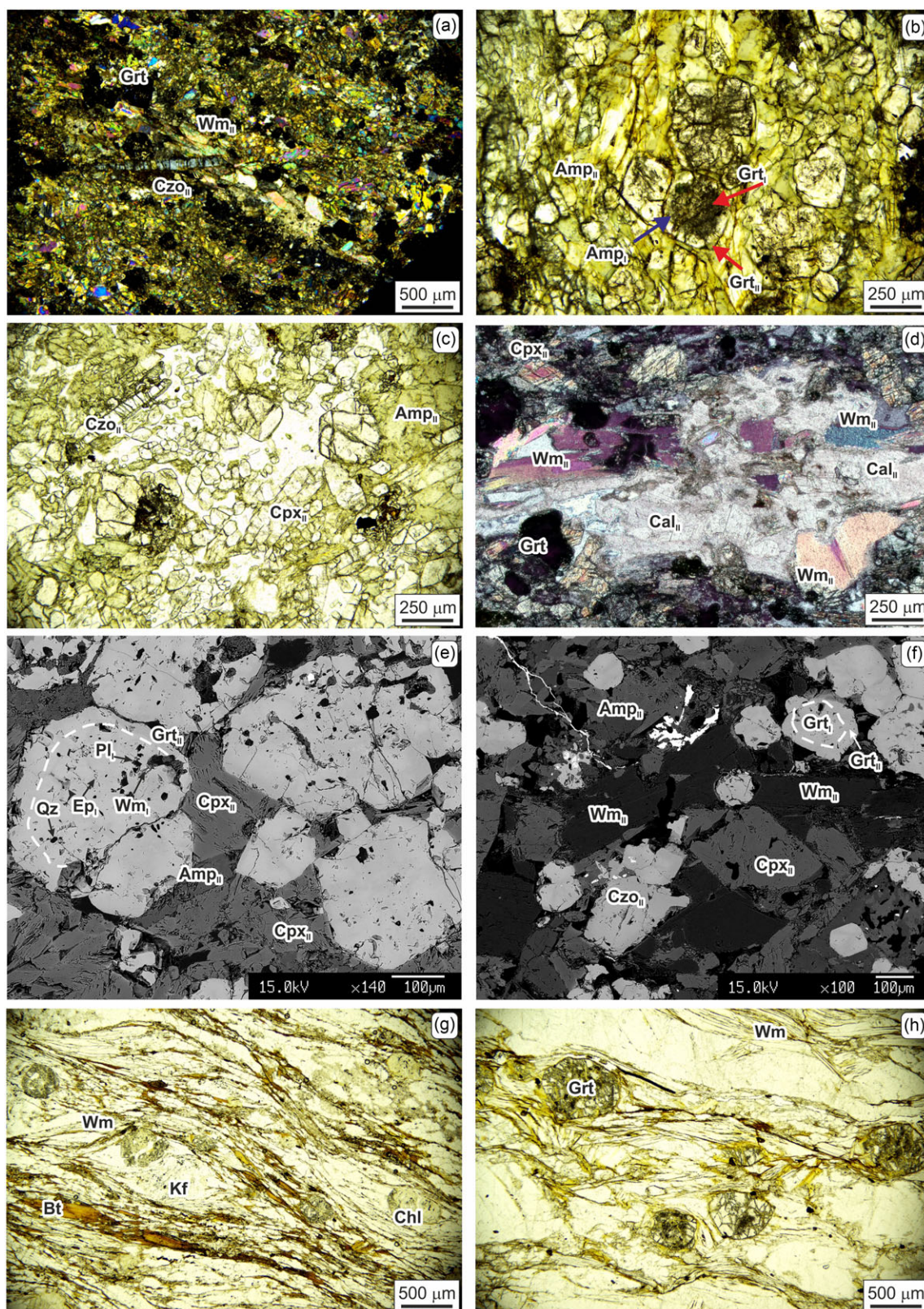
Figure 4. (Colour online) Microphotographs of rock fabrics. (a) The preserved eclogites showing an inequigranular texture, with garnet porphyroblasts of 5-12 mm embedded in a matrix; (b) Garnet porphyroblasts showing inclusions-rich core (Grt$_I$) and clear rim (Grt$_{II}$); (c) Clinozoisite (Czo$_{II}$) occurs along the HP foliation in retrogressed eclogite; (d) Cal$_{II}$ laths aligned parallel to the eclogitic foliation marked by Wm$_{II}$. Two-mica orthogneisses (g) and garnet-bearing paragneisses (h) showing a foliation made by micas enveloping feldspar (g) or garnet (h) porphyroblasts. (e) Garnet porphyroblasts preserving in their cores minerals of stage I (i.e. pre-eclogitic); (f) Stage II phase assemblage with Amp$_{II}$ + Wm$_{II}$ + Cpx$_{II}$ + Grt$_{II}$ + Czo$_{II}$.

Figure 5. Reconstructed textural equilibrium phase assemblages derived from microstructural observation for pre-eclogite (I), eclogite (II) and amphibolite (III) metamorphic evolution stages.

Figure 5) and (3) a late amphibolite-facies retrogression (stage III in Figure 5). Subscripts of mineral labels refer to the metamorphic stages in which they formed and/or were re-equilibrated.

5.a. Pre-eclogite facies stage (I)

Due to the strong overprint during subsequent deformation and metamorphic recrystallization, most of the mineral assemblages and textures belonging to the pre-eclogite facies metamorphism have been preserved only as inclusions in the cores of garnet porphyroblasts (Figure 5b). The preserved phase assemblage (Figure 5) is represented by:

$$Grt_I + Amp_I + Wm_I + Ep_I + Pl_I + Qz + Ilm_I.$$
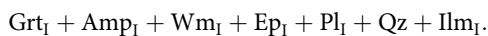
5.b. HP eclogite facies stage (II)

The eclogites display an inequigranular texture, with garnet porphyroblasts of 5-12 mm embedded in a matrix mainly composed of omphacite, amphibole and zoisite. Garnets have frequently an inclusions-rich core (Grt_I) and a clear rim (Grt_{II}).

The rim of garnet porphyroblasts (Grt_{II}) appears pre- to syn-kinematic with respect to the HP foliation (Figure 4b), which is individuated by the shape preferred orientation of omphacite (Cpx_{II}), amphibole (Amp_{II}) and white mica (Wm_{II}). Clinozoisite (Czo_{II}) also occurs along the HP foliation in some samples (Figure 4c) or crosscut the foliation (Czo_{III}). Calcite also occurs, in lath-shaped crystals parallel to the omphacite and white mica foliation (Figure 4d), likely derived from previous aragonite at HP and subsequently transformed into calcite during decompression (Dey *et al.* 2023). Tiny rutile crystals (Rt_{II}) occur mainly close to Amp_{II} or along omphacite-garnet interfaces.

The HP eclogite facies were constrained by the phase assemblage (Figure 5):

$$Grt_{II} + Cpx_{II} + Wm_{II} + Czo_{II} + Amp_{II} + Rt_{II} + Cal_{II} + Qz.$$
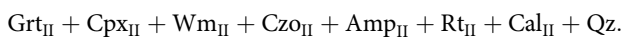
5.c. Amphibolite-facies stage (III)

The retrogression under amphibolites-facies conditions results in the partial substitution of omphacite (Cpx_{II}) by pseudomorphic aggregates of amphibole (Amp_{III}) + plagioclase (Pl_{III}) or diopside (Cpx_{III}) + plagioclase (Pl_{III}), which is evidence of the late partial breakdown of omphacite during water-present decompression after HP metamorphism (O'Brien & Rötzler, 2003; Martin, 2019). Extremely fine-grained diopside + hornblende + plagioclase symplectites grew after the HP Ca-Na-clinopyroxene (Cpx_{II}). The amphibole formed at this stage not only occurs in symplectites but also crystallizes in the matrix, partially substituting large Amp_{II} crystals with prismatic habit that were likely aligned along the HP foliation. Epidote (Ep_{III}) has been also observed in some samples. The phase assemblage (Figure 5) is represented by:

$$Amp_{III} + Pl_{III} + Cpx_{III} + Ep_{III} + Qz.$$
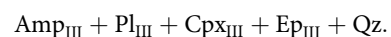
6. Mineral chemistry

Mineral phases representative of the crystallization/deformation stages reconstructed above were analysed to define the P-T conditions during the whole tectonometamorphic evolution of the NSMC.

X-rays elemental maps of garnet porphyroblasts (Figure 6) show a heterogeneous compositional variation. As shown in Figures 6c and 6d, the microstructural zoning characterized by inclusions-rich cores and clear rims reflects two crystallization events (Grt_I and Grt_{II}). Both Grt_I and Grt_{II} show a poorly developed chemical zonation, with only a very slight increase of pyrope from cores to rims (Figure 6b). Grossular and spessartine are grossly homogeneous (exception done for microinclusions of the pre-eclogitic stage revealed by some spots). At a closer view, spessartine shows a patchy variation possibly derived from dissolution-precipitation phenomena associated with the occurrence of fluids (e.g. Giuntoli *et al.* 2018; Hyppolito *et al.* 2019). Garnet porphyroblasts are frequently fractured, as well observable in the Ca and Mg maps of Figure 6, allowing the penetration of fluids inside them.
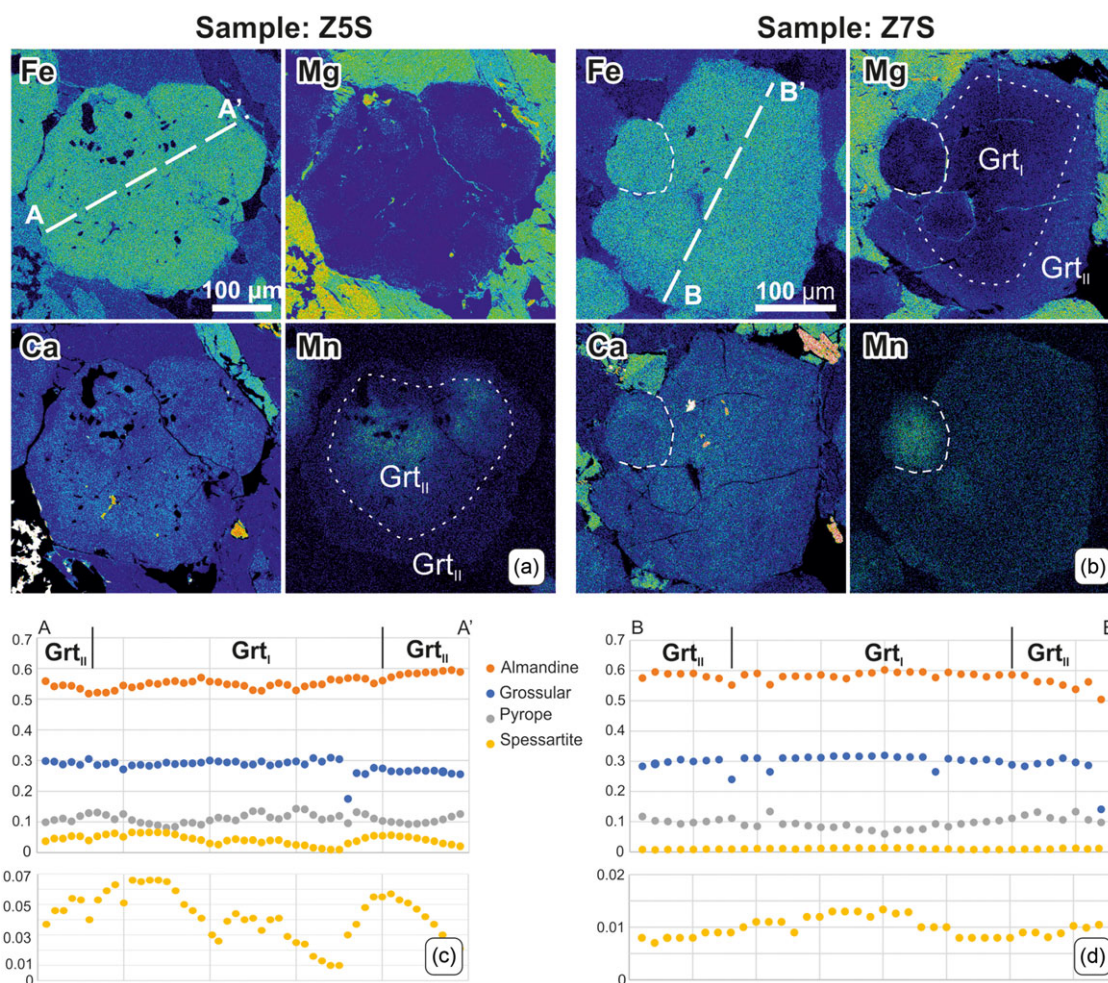
Figure 6. (Colour online) WDS X-ray elemental maps of representative garnet porphyroblasts of the NSMC eclogites. Mn-rich cores are visible in both garnet porphyroblasts from samples Z5S (a) and Z7S (b). If Z7S garnet displays a continuous zoning, garnet from sample Z5S displays a patchy zoning, with irregular distribution of Ca and Mn abundances (a). The compositional profile obtained by means of quantitative WDS spot analyses along a line of Figure 6c related to the Mn-content clearly points to a polyphasic growth of garnet porphyroblasts. In the lower part of (c) and (d) the spessartine content is shown with an enlarged vertical scale to see the Sps variation along the profile.

The chemical composition of garnets from eclogites could be summarized as follows: Grt_I (garnet cores) consists of $Alm_{52-58}Grs_{29-31}Pyr_{9-15}Sps_{1-7}$; Grt_{II} (garnet rims) consists of $Alm_{52-60}Grs_{24-30}Pyr_{10-13}Sps_{0-3}$ (representative EMPA of garnets are reported in Table 2).

Pre-eclogitic stage mineral phases are only preserved as inclusions in garnet cores (Grt_I). Among them, phengitic white mica (Wm_I) and amphibole (Amp_I) are the most useful for the determination of P-T conditions during this stage. Wm_I has a phengitic composition with Si contents ranging from 3.34 to 3.36 atoms per formula units (a.p.f.u.). Amphiboles included in garnet cores (Amp_I) are sodic-calcic, with Si of 6.6-6.7 a.p.f.u. Following the classification scheme of Hawthorne & Oberti (2007), they could be classified as magnesio-katophorites. Other minerals of the same stage are epidote (Ep_I), an almost pure pistacite (Table 2), quartz, ilmenite, and rare plagioclase (Pl_I) displaying an albitic composition (Table 3). The observed microstructural relationships do not allow to assess if garnet was a stable phase during this stage (as proposed in Figure 5) or grew later, following increasing pressure conditions that lead to the eclogitic stage (Stage II, Figure 5).

Cpx_{II} displays composition with a Na content expressed as jadeite from 0.36 to 0.46 mol% (Table 3), with increasing Na from core to rim (Figure 7a), resembling the prograde zonation of garnet.

The shape preferred orientation of Cpx_{II}, and Wm_{II} defines the eclogitic foliation. Wm_{II} has higher Si content with respect to Wm_I (Figure 7b), suggesting higher pressure conditions. The Si content of Wm_{II} ranges from 3.36 to 3.40 a.p.f.u., approaching the celadonitic end member. Rare Amp_{II} crystals in eclogite, stable with the other HP mineral phases, also display compositions in agreement with the magnesio-katophorite compositional field (Figure 7d) like Amp_I, but with slightly lower Si contents and X_{Mg} [$Mg/(Mg+Fe^{2+})$] values.

Eclogites of the NSMC are partially to completely retrogressed under amphibolites-facies conditions. Samples displaying the most complete retrogression during this stage were selected for EMPA. The Amp_{III} partially replaces Amp_{II} corresponding to a Mg-hornblende (Figure 7c) and its composition significantly differs from previous amphibole generation, becoming more Ca-rich (Figure 7c), plotting within the magnesio-hornblende field. The Na content of Amp_{III} is lower (0.42-0.45 a.p.f.u.) with respect to Amp_{II}, suggesting that they likely formed already during the exhumation after the pressure peak. Amp_{II}, growing both at the expense of Amp_I and in the matrix, has lower Ca and Si (6.15-6.25 a.p.f.u.). Fe-rich epidote (Ep_{III}) is the Al-rich phase in place of garnet, suggesting lower pressure conditions during this stage, i.e. epidote-amphibolite facies.

Table 2. Representative EMPA of Grt porphyroblasts of the NSMC eclogites. (I) Garnet cores, (II) garnet rims

Mineral	Grt$_I$ (core)						Grt$_{II}$ (rim)					
Sample	Z5S	Z5S	Z5S	Z7S	Z7S	Z7S	Z5S	Z5S	Z5S	Z7S	Z7S	Z7S
SiO$_2$	38.63	38.45	38.57	40.66	38.5	38.38	38.21	38.73	38.66	39.02	38.79	38.88
TiO$_2$	0.17	0.16	0.18	0.11	0.18	0.13	0.16	0.07	0.15	0.2	0.24	0.18
Al$_2$O$_3$	21.33	21.46	21.6	19.04	21.18	21.2	21.47	21.44	21.23	21	20.85	20.81
Cr$_2$O$_3$	0	0	0	0.01	0.02	0	0	0.04	0.05	0.06	0	0
FeO†	23.9	23.95	23.91	27.88	26.93	27.25	26.26	27.12	26.78	25.25	25.89	26.13
MnO	2.42	2.68	2.82	0.65	0.57	0.63	0.38	0.32	0.35	2.47	2.54	2.35
MgO	3.38	3.18	2.77	1.55	1.88	1.87	3.01	2.63	2.58	2.61	2.54	2.48
CaO	10.43	10.57	10.64	11.67	11.3	11.4	10.56	10.48	10.75	9.91	9.65	9.51
Na$_2$O	0.07	0.05	0.02	0.01	0	0	0.06	0.02	0	0	0	0
K$_2$O	0.02	0	0	0	0	0.01	0	0	0	0	0.01	0
Total	100.35	100.49	100.51	101.58	100.56	100.87	100.34	100.85	100.54	100.52	100.51	100.35
Si	3.02	3.01	3.02	3.19	3.03	3.02	3.00	3.03	3.04	3.07	3.06	3.07
Ti	0.01	0.01	0.01	0.01	0.01	0.01	0.01	0.00	0.01	0.01	0.01	0.01
Al	1.97	1.98	1.99	1.76	1.97	1.96	1.98	1.98	1.97	1.95	1.94	1.94
Cr	0.00	0.00	0.00	0.00	0.00	0.00	0.00	0.00	0.00	0.00	0.00	0.00
Fe^{2+}	1.56	1.57	1.57	1.83	1.77	1.79	1.72	1.77	1.76	1.66	1.71	1.73
Mn	0.16	0.18	0.19	0.04	0.04	0.04	0.03	0.02	0.02	0.16	0.17	0.16
Mg	0.39	0.37	0.32	0.18	0.22	0.22	0.35	0.31	0.30	0.31	0.30	0.29
Ca	0.87	0.89	0.89	0.98	0.95	0.96	0.89	0.88	0.90	0.84	0.82	0.80
Na	0.01	0.01	0.00	0.00	0.00	0.00	0.01	0.00	0.00	0.00	0.00	0.00
Grossular	0.29	0.29	0.29	0.32	0.31	0.31	0.28	0.29	0.30	0.27	0.27	0.26
Almandine	0.52	0.52	0.53	0.60	0.59	0.60	0.58	0.60	0.59	0.56	0.57	0.58
Pyrope	0.13	0.12	0.11	0.06	0.07	0.07	0.12	0.10	0.10	0.10	0.10	0.10
Spessartite	0.05	0.06	0.06	0.01	0.01	0.01	0.01	0.01	0.01	0.06	0.06	0.05

†Total iron as FeO.

7. ^{40}Ar/^{39}Ar geochronology

Two samples have been investigated for the determination of the geochronological evolution of the NSMC (Figure 8 and Table 4). White mica separates from an eclogite (sample Z7S) and amphibole (Amp$_{III}$) from an amphibolite (Z3S) have been analysed for ^{40}Ar/^{39}Ar dating in order to constrain the timing of the peak pressure and the subsequent retrogression at epidote-amphibolites-facies conditions.

White mica (Wm$_{II}$) grows aligned along the eclogitic foliation, so its recrystallization age broadly corresponds to the HP peak stage experienced by the NSMC eclogites. Taking into consideration the flat part of the age spectrum corresponding to homogeneous Ca/K values calculated from the ^{37}Ar/^{39}Ar ratio (Figure 8) and the amount of gas released in the flat part of the spectrum, which corresponds to c. 84% of the total ^{39}Ar released, the age of white mica in Z7S is 191.14 ± 0.50 Ma (Figure 8a, b).

Large amphibole crystals belonging to the Amp$_{III}$ generation in completely retrogressed eclogites (i.e. amphibolite) have been selected for dating. The Ar release pattern of the Z3S sample (Figure 8c) is quite complex. The staircase pattern is likely related to the mixing trend of two amphibole generations, Amp$_{II}$ and Amp$_{III}$, the latter partially overgrown at the expenses of Amp$_{II}$

(see above), showing different Ca/K ratios (Figure 8d). Considering the chemical composition derived from the ^{37}Ar/^{38}Ar, the cluster showing lower Ca/K ratios is referred to be 143.96 ± 5.82 Ma, whereas the cluster with higher Ca/K ratios has 194.38 ± 4.30 Ma. This age distribution accounts for the stability of amphibole during peak pressure condition and subsequent recrystallization with decreasing Ca/K ratio during retrogression. EMPA data indicate that Amp$_{III}$ has significantly lower Ca/K values with respect to Amp$_{II}$ (Table 3).

8. Thermodynamic modelling and metamorphic evolution

The microstructural analyses and the chemical composition of HP minerals in the studied (not retrogressed) eclogites indicate a prograde metamorphism mainly recorded by two stages of garnet crystallization (core, Grt$_I$, and rim, Grt$_{II}$), and a subsequent chemical zoning observed both in garnet rims (Grt$_{II}$) and in omphacite (Cpx$_{II}$). Moreover, the patchy garnet zoning (Figure 6c) was likely due to syn-deformation dissolution and reprecipitation processes mediated by metamorphic fluids. This is evidence of a complex metamorphic history that is difficult to reconstruct in detail from a thermodynamic modelling point of view.

Table 3. Representative EMPA of Cpx, Wm, Amp, Ep, and Pl of the NSCM eclogites. (I) pre-eclogite, (II) eclogite and (III) amphibolite metamorphic evolution stages

Mineral	Cpx$_{II}$							Cpx$_{III}$		Wm$_I$					Wm$_{II}$						
Sample	Z5S	Z5S	Z5S	Z5S	Z5S	Z5S	Z5S	Z3S	Z3S	Z5S	Z5S	Z5S	Z5S	Z5S	Z3S	Z3S	Z3S	Z5S	Z5S	Z5S	Z5S
SiO$_2$	56.63	56.71	56.83	56.60	56.83	56.98	56.20	53.61	53.45	50.79	51.08	50.81	50.91	50.82	51.42	52.36	52.37	53.09	52.54	52.16	52.28
TiO$_2$	0.12	0.09	0.09	0.12	0.07	0.09	0.01	0.17	b.d.l.	0.53	0.53	0.50	0.52	0.55	0.54	0.61	0.61	0.59	0.49	0.56	0.57
Al$_2$O$_3$	10.46	8.82	10.08	9.39	10.79	10.00	9.12	0.87	0.99	29.66	29.03	29.34	29.12	29.56	28.89	29.55	29.95	29.77	29.42	29.24	29.66
Cr$_2$O$_3$	0.03	0.04	0.04	0.04	0.03	0.06	b.d.l.	b.d.l.	b.d.l.	b.d.l.	0.07	0.01	0.02	0.01	0.02	0.03	b.d.l.	0.04	b.d.l.	0.01	0.03
FeO†	5.13	5.55	5.61	4.12	4.21	4.33	4.99	8.31	9.16	2.07	2.37	2.14	2.35	2.24	1.81	1.66	1.59	1.66	1.59	1.77	1.71
MnO	0.00	0.02	0.03	0.01	0.00	0.05	0.02	0.24	0.11	0.01	0.07	0.07	0.07	0.03	0.05	b.d.l.	0.02	b.d.l.	b.d.l.	b.d.l.	0.01
MgO	8.19	9.01	7.95	9.29	7.87	8.47	9.09	13.04	12.06	2.81	2.87	2.84	2.87	2.86	3.05	3.12	3.10	2.92	3.05	3.02	3.11
CaO	13.79	15.04	14.08	15.47	13.59	14.43	15.09	23.58	23.69	0.02	0.02	0.02	0.01	0.01	b.d.l.	0.02	0.01	0.02	b.d.l.	0.01	0.03
Na$_2$O	6.81	5.74	6.66	5.51	6.64	6.38	5.73	0.31	0.59	0.89	0.84	0.81	0.82	0.84	0.81	0.69	0.75	0.72	0.68	0.69	0.68
K$_2$O	0.01	b.d.l.	b.d.l.	b.d.l.	b.d.l.	b.d.l.	0.01	0.01	b.d.l.	8.85	8.86	8.89	8.99	8.89	9.08	9.02	9.46	9.09	9.33	8.88	9.23
Total	101.17	101.02	101.37	100.55	100.03	100.79	100.26	100.14	100.05	95.63	95.74	95.43	95.68	95.81	95.67	97.06	97.86	97.90	97.10	96.34	97.31
Si	1.99	2.01	2.00	2.01	2.01	2.01	2.00	2.00	2.00	3.31	3.33	3.32	3.32	3.31	3.35	3.35	3.34	3.37	3.37	3.36	3.35
Ti	0.00	0.00	0.00	0.00	0.00	0.00	0.00	0.01	–	0.03	0.03	0.02	0.03	0.03	0.03	0.03	0.03	0.03	0.02	0.03	0.03
Al	0.43	0.37	0.42	0.39	0.45	0.42	0.38	0.04	0.05	2.28	2.23	2.26	2.24	2.27	2.22	2.23	2.25	2.23	2.23	2.22	2.24
Cr	0.00	0.00	0.00	0.00	0.00	0.00	–	–	–	–	0.00	0.00	0.00	0.00	0.00	0.00	–	–	–	–	0.00
Fe^{3+}	0.04	0.03	0.04	0.00	0.01	0.02	0.01	0.00	0.00	0.00	0.00	0.00	0.00	0.00	0.00	0.00	0.00	0.00	0.00	0.00	0.00
Fe^{2+}	0.11	0.13	0.13	0.12	0.12	0.10	0.13	0.26	0.29	0.11	0.13	0.12	0.13	0.12	0.10	0.09	0.08	0.09	0.09	0.10	0.09
Mn	0.00	0.00	0.00	0.00	0.00	0.00	0.00	0.00	0.01	0.00	0.00	0.00	0.00	0.00	0.00	–	0.00	–	–	–	0.00
Mg	0.43	0.48	0.42	0.49	0.42	0.45	0.48	0.72	0.67	0.27	0.28	0.28	0.28	0.28	0.30	0.30	0.29	0.28	0.29	0.29	0.30
Ca	0.52	0.57	0.53	0.59	0.52	0.55	0.58	0.94	0.95	0.00	0.00	0.00	0.00	0.00	–	0.00	0.00	0.00	0.00	0.00	0.00
Na	0.47	0.39	0.45	0.38	0.46	0.44	0.40	0.02	0.04	0.11	0.11	0.10	0.10	0.11	0.10	0.09	0.09	0.09	0.08	0.09	0.08
K	0.00	–	–	–	–	–	–	–	–	0.74	0.74	0.74	0.75	0.74	0.76	0.74	0.77	0.74	0.76	0.73	0.75
Cation Sum	4.00	3.99	3.99	3.98	3.98	3.99	4.00	3.99	4.01	6.85	6.84	6.85	6.85	6.84	6.86	6.82	6.86	6.83	6.85	6.82	6.84
X$_{Mg}$=(Mg/Mg+Fe^{2+})	0.79	0.78	0.77	0.80	0.78	0.81	0.78	0.74	0.70	0.71	0.68	0.70	0.69	0.70	0.75	0.77	0.78	0.76	0.77	0.75	0.76
Al$^{(IV)}$	0.01	0.00	0.00	0.00	0.00	0.00	0.00	0.00	0.00	1.59	1.56	1.58	1.56	1.57	1.57	1.58	1.59	1.61	1.60	1.59	1.58
Al$^{(VI)}$	0.43	0.37	0.42	0.39	0.45	0.42	0.38	0.04	0.05	1.00	1.00	1.00	1.00	1.00	1.00	1.00	1.00	1.00	1.00	1.00	1.00

Mineral	Amp$_I$			Amp$_{II}$					Amp$_{III}$			Ep$_I$				Pl$_I$		Pl$_{III}$
Sample	Z3S	Z5S	Z5S	Z3S	Z3S	Z3S	Z5S	Z5S	Z3S	Z3S	Z3S	Z3S	Z3S	Z7S	Z7S	Z5S	Z3S	Z5S
SiO$_2$	46.37	45.98	46.44	51.21	50.36	49.22	49.02	49.93	47.54	42.14	47.63	39.45	39.15	39.72	39.42	68.81	68.66	60.91
TiO$_2$	0.42	0.38	0.43	0.36	0.39	0.37	0.46	0.72	0.38	0.28	0.38	0.18	0.09	0.09	0.03	b.d.l.	b.d.l.	b.d.l.
Al$_2$O$_3$	14.68	14.69	14.59	11.69	11.96	11.86	12.26	11.78	11.86	19.10	12.15	29.56	28.10	29.37	28.55	19.63	19.67	25.08
Cr$_2$O$_3$	b.d.l.	b.d.l.	b.d.l.	0.01	0.06	0.02	b.d.l.	0.05	0.11	0.04	0.05	b.d.l.	0.03	b.d.l.	0.01	0.03	0.00	0.02
FeO†	12.10	12.11	12.01	8.86	9.26	11.23	11.18	10.54	12.63	15.00	12.63	6.11	7.50	6.11	7.39	0.27	0.29	0.41
MnO	0.11	0.12	0.10	0.11	0.14	0.11	0.05	0.05	0.25	0.23	0.20	0.25	0.19	0.11	0.26	0.00	0.07	0.00

(Continued)

Table 3. (*Continued*)

Mineral	Amp$_I$			Amp$_{II}$					Amp$_{III}$			Ep$_I$				Pl$_I$		Pl$_{III}$
Sample	Z3S	Z5S	Z5S	Z3S	Z3S	Z3S	Z5S	Z5S	Z3S	Z3S	Z3S	Z3S	Z3S	Z7S	Z7S	Z5S	Z3S	Z5S
MgO	11.37	11.31	11.38	14.18	13.81	12.34	12.60	12.66	12.14	8.70	12.47	0.07	0.06	0.08	0.00	0.01	b.d.l.	b.d.l.
CaO	9.42	9.54	9.45	8.85	9.07	9.05	9.05	9.06	11.53	11.05	11.90	23.49	23.17	23.50	23.02	0.31	0.36	5.90
Na$_2$O	3.41	3.32	3.45	2.96	3.02	3.57	3.61	3.34	1.58	2.04	1.61	b.d.l.	b.d.l.	b.d.l.	0.01	10.99	10.92	7.87
K$_2$O	0.48	0.43	0.45	0.35	0.38	0.44	0.42	0.38	0.21	0.45	0.19	b.d.l.	b.d.l.	b.d.l.	0.01	0.07	0.10	0.06
Total	98.36	97.88	98.30	98.58	98.45	98.21	98.65	98.51	98.23	99.03	99.21	99.11	98.29	98.98	98.70	100.12	100.07	100.25
Si	6.61	6.59	6.63	7.09	7.02	7.00	6.93	7.05	6.81	6.05	6.76	2.99	3.01	3.02	3.01	3.02	3.02	2.71
Ti	0.04	0.04	0.05	0.04	0.04	0.04	0.05	0.08	0.04	0.03	0.04	0.01	0.01	0.00	0.00	–	–	–
Al	2.47	2.48	2.45	1.91	1.97	1.99	2.04	1.96	2.00	3.23	2.03	2.64	2.54	2.63	2.57	1.02	1.02	1.31
Cr	–	–	–	0.00	0.01	0.00	–	0.01	0.01	0.01	0.01	–	0.00	–	0.00	0.00	0.00	0.00
Fe^{3+}	0.30	0.32	0.26	0.36	0.31	0.10	0.20	0.07	0.27	0.57	0.26	0.39	0.48	0.39	0.47	0.00	0.00	0.00
Fe^{2+}	1.14	1.13	1.17	0.67	0.77	1.24	1.12	1.18	1.24	1.23	1.24	0.00	0.00	0.00	0.00	0.01	0.01	0.02
Mn	0.01	0.01	0.01	0.01	0.02	0.01	0.01	0.01	0.03	0.03	0.02	0.01	0.01	0.01	0.02	0.00	0.00	0.00
Mg	2.42	2.42	2.42	2.93	2.87	2.62	2.65	2.66	2.59	1.86	2.64	0.01	0.01	0.01	0.00	0.00	–	–
Ca	1.44	1.47	1.45	1.31	1.36	1.38	1.37	1.37	1.77	1.70	1.81	1.91	1.91	1.91	1.88	0.01	0.02	0.28
Na	0.94	0.92	0.96	0.79	0.82	0.98	0.99	0.91	0.44	0.57	0.44	–	–	–	0.00	0.94	0.93	0.68
K	0.09	0.08	0.08	0.06	0.07	0.08	0.07	0.07	0.04	0.08	0.03	–	–	–	0.00	0.00	0.01	0.00
Cation Sum	15.47	15.47	15.48	15.17	15.24	15.44	15.43	15.35	15.25	15.35	15.29	7.97	7.97	7.97	7.96	5.00	5.00	5.00
X$_{Mg}$=(Mg/Mg+Fe^{2+})	0.68	0.68	0.67	0.81	0.79	0.68	0.70	0.69	0.68	0.60	0.68	0.65	0.55	0.63	0.57	0.02	0.02	0.29
Al$^{(IV)}$	1.39	1.41	1.37	0.91	0.98	1.00	1.07	0.95	1.19	1.95	1.24	0.35	0.45	0.37	0.43	0.98	0.98	0.70
Al$^{(VI)}$	1.08	1.08	1.09	1.00	0.99	0.99	0.97	1.01	0.81	1.28	0.79							

†Total iron as FeO; b.d.l.: below detection limit.

https://doi.org/10.1017/S0016756824000098 Published online by Cambridge University Press

C Montemagni *et al.*
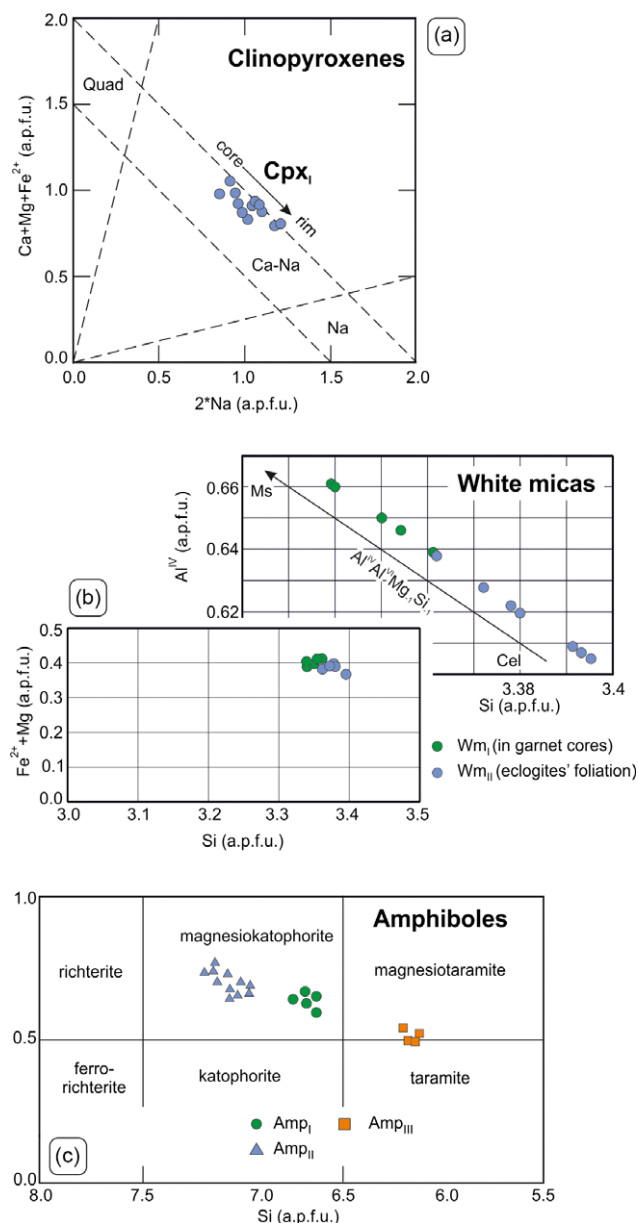
Figure 7. (Colour online) (a) Clinopyroxene (Cpx_{II}) composition, rims are enriched in Na. (b) The Si content of phengitic white micas increases from Wm_I, preserved as inclusion in garnet cores to Wm_{II} stable as HP phase. (c) Classification of Ca-Na amphibole composition in eclogites and amphibolites, see text for description.

Conventional geothermobarometric calculations have been performed on one of the best-preserved eclogites (Z5S) in order to compare the obtained estimates with the modelling results (e.g. Wei & Clarke, 2011). The occurrence of coexisting clinopyroxene and garnet stable in the peak metamorphic assemblage (Stage II) allows the use of the Fe-Mg exchange thermometer (Krogh Ravna, 1988, 2000) between the two phases. The occurrence of phengite also allows estimating the pressure using the geothermobarometer of Krogh Ravna & Terry (2004) developed for garnet + omphacite + phengite + kyanite + quartz in the KCMASH system. In the quartz stability field, the geothermobarometer consists of three independent reactions cross-cutting each other in a single invariant point (Figure 9a). One of the three reactions is kyanite and quartz-free (2 Grs + Pyr + 3 Al-Cel = 6 Di + 3 Mus), therefore suitable for the kyanite-free eclogites of the NSCM. Minerals (garnet,

omphacite and phengite) in textural equilibrium showing no sign of retrogression have been selected and analysed with the EMP (Table 5), and the results are reported in Figure 9a and Table 5. The estimated pressure ranges from 1.90 to 2.15 GPa with T in the 510-600 °C using the Krogh Ravna (1988) thermometer. A restricted temperature interval, 510-540 °C, stems instead employing the Krogh Ravna (2000) version of the same thermometer.

With respect to conventional geothermobarometry, the reconstruction using forward modelling is in principle more robust even if the limitations of reliable solid solution models, particularly of amphibole, must be kept into consideration.

In order to check the role of CO_2 in the fluid and the stability of carbonates at the peak pressure as shown by the microstructural evidences, we constructed a T-X section of sample S5Z, based on the variation of $X(CO_2)$ and temperature, at P = 2 GPa (Figure 9b).

The amount of CO_2 strongly influences the stability of zoisite in a short range of temperature (550 – 650 °C, at $X(CO_2)$ up to 0.3). We therefore considered the phase assemblage garnet, omphacite, carbonate, quartz, zoisite, and rutile (± amphibole) as the possible mark of P-T range at $X(CO_2)$ up to 0.1, as demonstrated by microstructural evidences. The occurrence of amphibole strongly influences the temperature range of the mineral stability (550-600 °C for $X(CO_2)$ = 0.01-0.04 or 550-650 °C for $X(CO_2)$ = 0.015-0.03). If we assume that amphibole was in equilibrium at the peak and compare the garnet mol% compositions with those retrieved by the thermodynamic modelling (see properties in the Supplementary Material 1), we estimate that the peak P-T conditions recorded by our preserved eclogites range from 550 to 600 °C, at 2 GPa.

9. Discussion

9.a. P-T conditions of metamorphism

The studied samples show peak mineral assemblage and garnet composition compatible with pressures in the range between 1.8 and 2.1 GPa (Figure 9a), considering the conventional thermobarometry. More difficult is the determination of the equilibration temperature that ranges between 500 °C and 650 °C based on the occurrence of CO_2 in the fluid that may or may not stabilize carbonates among the HP mineral assemblages, along with the stability of amphibole at peak conditions. In addition, the comparison with experimental works on the phase stability of amphibole + zoisite in mafic assemblages (e.g. Schmidt & Poli, 1998; Forneris & Holloway, 2003) is in agreement with both the estimated temperatures, being stable between 500 and 700 °C. It must be noted that even if the bulk composition of our studied samples is slightly depleted in SiO_2 (46.71 vs 52.4 wt%) and enriched in MgO (8.30 vs 7.1 wt%) with respect to a MORB as reported in the experiments of Schmidt & Poli (1998), in the presence of fluids our phengite-bearing eclogites would have undergone partial melting at 1.8 GPa and 700 °C. The presence of fluids at peak conditions is demonstrated not only by the occurrence of hydrous phases but also by the microstructure of garnet zoning that resembles a coupled dissolution-reprecipitation and diffusional equilibration (Figure 6; Massonne & Li, 2020). However, the microstructures of our samples do not give evidence of such high temperatures and/or related symplectites growing during the retrogression, such as those encountered in the Central Italian Alps, at Borgo (Pellegrino et al. 2020).

The conditions of the formation of amphibole and clinozoisite-epidote porphyroblasts in eclogites have only rarely been addressed (Massonne, 2012 with references), but P-T conditions around
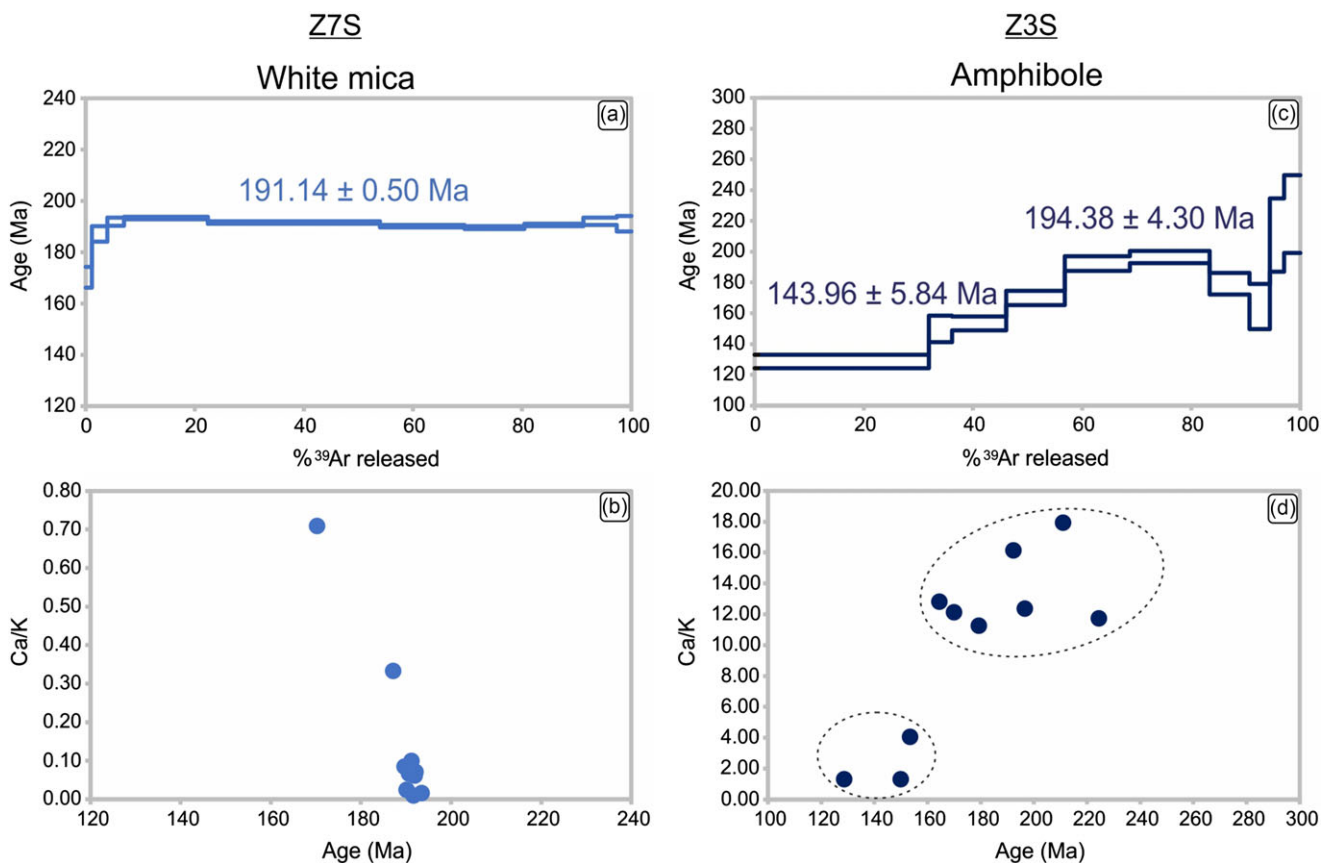
Figure 8. (Colour online) $^{40}Ar/^{39}Ar$ age spectra and Ca/K vs. age diagrams for eclogite Z7S (a, b) and amphibolite Z3S (c, d). Dotted circles in (d) are referred to amphibole generations Amp_{II} and Amp_{III}.

2 GPa and 600 °C seem to be characteristic for their formation. These P estimates are similar to our data within the analytical error. Massonne (2012) suggested that the formation of amphibole and clinozoisite in eclogite is typical in subduction settings where deep burial of material from the overriding plate occurred, followed by fluid infiltration responsible for the formation of H_2O-bearing HP mineral phases in former anhydrous phase assemblages. After the first hydration, the formation of hydrous porphyroblasts in HP rocks can continue also during their progressive exhumation, following resorption and compositional re-equilibration of existing porphyroblasts and the growth of new ones when the destabilization of hydrous phases occurs in response of P-T variations (e.g. Huang *et al.* 2020, 2023) in dynamic settings like subduction channels.

The eclogites from Dabie Shan in China (Massonne, 2012), Altiplano-Puna plateau in the central Andes (Allmendinger *et al.* 1997; Giese *et al.* 1999), Kaghan Valley in western Himalaya (Lombardo & Rolfo, 2000; Wilke et al. 2010), Cretaceous eclogites from the Austroalpine domain of the European Alps (e.g. Spalla *et al.* 1996; Thöni, 2006; Zanchetta *et al.* 2013b) may represent a geodynamic scenario similar to the one given by the eclogites of the North Shahrekord Metamorphic Complex. The clockwise P-T path (Figure 10d) constructed for the eclogite accounts for an initial pre-eclogite stage (stage I) preserved in garnet porphyroblasts, a HP eclogite facies metamorphic stage at 1.90-2.15 GPa and 550-600 °C and a subsequent epidote-amphibolite-facies retrograde stage. The estimated peak conditions fall for temperature in the range (470-630°C) proposed by Davoudian *et al.* (2008) and
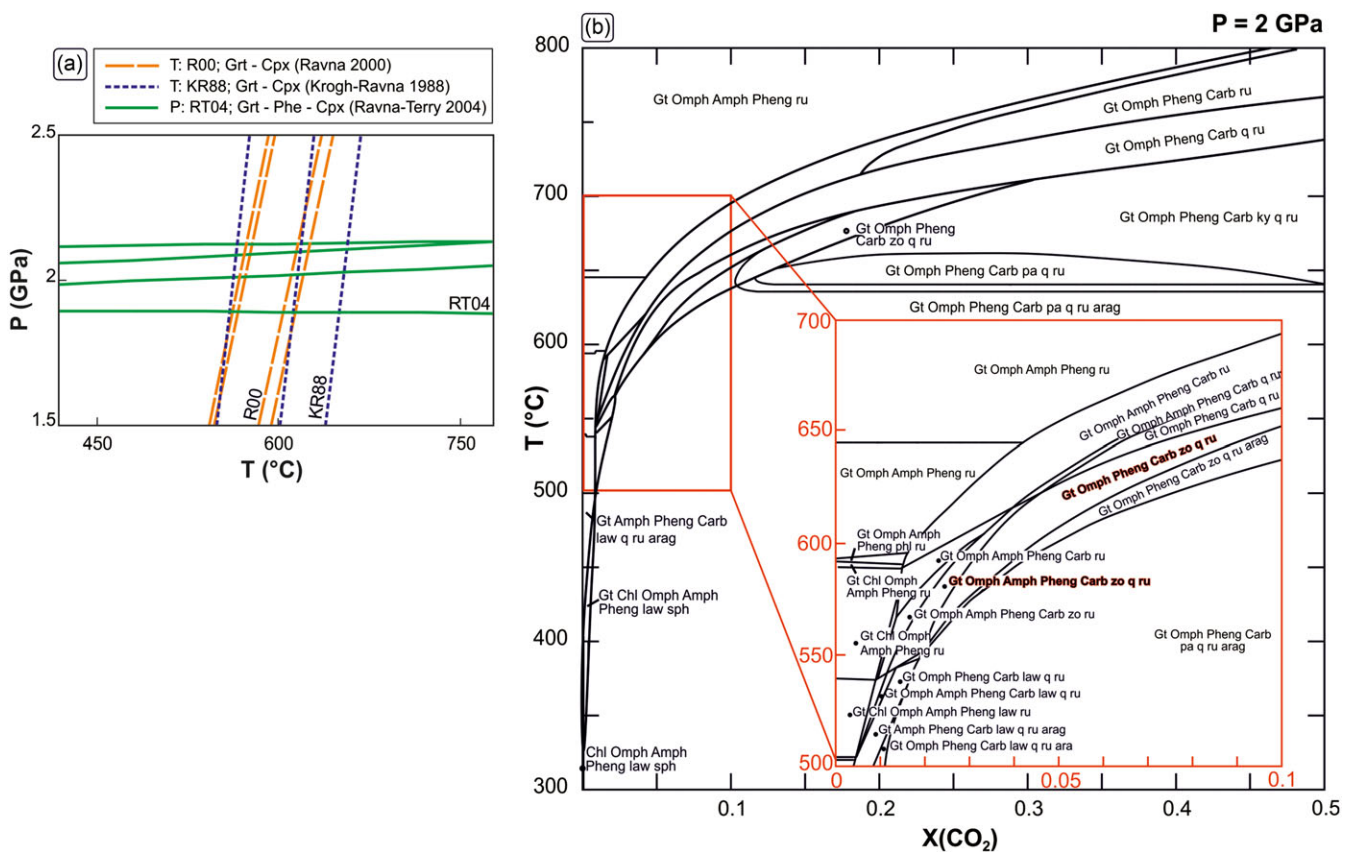
Davoudian *et al.* (2016) for the same NSMC eclogites. Our estimated pressures are instead lower by about 0.4-0.6 GPa, as previously calculated pressures are high as 2.5 GPa (Davoudian *et al.* 2008; Davoudian *et al.* 2016). We suggest that this higher pressures should be considered only as a maximum as a) the used chemical composition of HP phases was selected to maximize the Na content in omphacite, the Si content in phengite, and the Pyr and Grs activity in garnet; b) the equilibrium phase assemblage on which the used geothermobarometer (Krogh Ravna & Terry, 2004) considers the occurrence of kyanite, which is not present in the NSMC eclogites; c) the occurrence of carbonates (calcite and dolomite, Davoudian *et al.* 2016) has not been considered in the geothermobarometric calculations. Regarding these last points, we would stress how the occurrence of a fluid phase not formed only by pure H_2O could significantly change the equilibrium phase assemblages as well as the composition of single minerals, as discussed before and shown in Figure 9b.

9.b. Timing and tectonic implications

The eclogites of the NSMC in the SSZ are the only record of Jurassic HP metamorphism identified in the Zagros orogen *sensu lato* (Davoudian *et al.* 2016), therefore being key rocks to the understanding of subduction-related processes that occurred in this area. The first question is if the $^{40}Ar/^{39}Ar$ is a sound method to date the metamorphic peak in HP assemblage or if inherited Ar and fluid-aided retrogression could affect the Ar retention or loss. Besides the fact that many workers endeavoured to date HP and

Table 4. $^{40}Ar/^{39}Ar$ data. All Ar isotope concentrations are given as mL. K, Ca and Cl concentrations are calculated from the sample mass and the ^{39}Ar, ^{37}Ar and ^{38}Ar concentrations, respectively. $^{40}Ar^{*}$=radiogenic ^{40}Ar. All errors are 1σ

Sample	Step #	^{40}Ar Tot	Err.^{40}Ar	$^{40}Ar^{*}$	Err.$^{40}Ar^{*}$	^{39}Ar	Err.^{39}Ar	%^{39}Ar	^{38}Ar	Err.^{38}Ar	$^{38}ArCl$	Err.^{38}Cl	^{37}Ar	Err.^{37}Ar	^{36}Ar	Err.^{36}Ar	Age	1σ Err	Ca/K	Error Ca/K	Cl/K	Error Cl/K
Z7S	1	1.79E-08	4.50E-12	4.22E-09	2.65E-11	4.11E-11	4.20E-13	1.17E+00	1.37E-11	1.90E-14	4.69E-12	4.48E-14	1.50E-11	5.67E-14	4.57E-11	8.74E-14	170.27	2.04	0.70925	0.00772	0.02029	0.00028
J= 0.000965	2	5.19E-08	2.10E-11	1.13E-08	7.92E-11	9.95E-11	3.92E-13	2.83E+00	2.95E-11	3.53E-14	2.80E-12	6.03E-14	1.71E-11	5.87E-14	1.36E-10	2.56E-13	187.17	1.51	0.33293	0.00174	0.00500	0.00011
m= 0.00616 g	3	1.67E-08	3.60E-12	1.25E-08	9.60E-12	1.07E-10	4.23E-13	3.05E+00	4.32E-12	1.02E-14	5.28E-13	7.14E-14	3.38E-12	4.96E-14	1.41E-11	2.98E-14	191.92	0.77	0.06126	0.00093	0.00088	0.00012
	4	6.82E-08	3.60E-11	6.33E-08	3.75E-11	5.39E-10	5.66E-13	1.54E+01	1.04E-11	1.78E-14	1.54E-12	5.25E-14	4.33E-12	5.00E-14	1.67E-11	3.52E-14	193.45	0.24	0.01558	0.00018	0.00051	0.00002
	5	1.33E-07	9.90E-11	1.28E-07	9.96E-11	1.11E-09	1.25E-12	3.15E+01	1.74E-11	2.92E-14	2.58E-12	5.31E-14	5.21E-12	5.07E-14	1.66E-11	3.65E-14	191.64	0.26	0.00913	0.00009	0.00042	0.00001
	6	6.86E-08	3.30E-11	6.27E-08	3.53E-11	5.44E-10	5.67E-13	1.55E+01	1.09E-11	1.91E-14	1.49E-12	5.37E-14	6.99E-12	5.11E-14	1.95E-11	4.21E-14	190.19	0.23	0.02491	0.00018	0.00049	0.00002
	7	5.10E-08	1.71E-11	4.44E-08	2.18E-11	3.86E-10	5.11E-13	1.10E+01	9.45E-12	1.64E-14	1.22E-12	5.30E-14	1.69E-11	5.81E-14	2.21E-11	4.50E-14	189.69	0.27	0.08474	0.00031	0.00056	0.00002
	8	5.56E-08	2.31E-11	4.37E-08	3.27E-11	3.78E-10	4.26E-13	1.08E+01	1.27E-11	2.03E-14	1.21E-12	5.03E-14	1.31E-11	5.60E-14	3.99E-11	7.76E-14	190.70	0.26	0.06715	0.00030	0.00057	0.00002
	9	5.06E-08	5.40E-11	2.51E-08	7.44E-11	2.16E-10	4.60E-13	6.15E+00	1.92E-11	3.12E-14	8.90E-13	5.87E-14	7.92E-12	5.23E-14	8.53E-11	1.71E-13	192.14	0.70	0.07119	0.00049	0.00073	0.00005
	10	4.80E-08	2.43E-11	1.08E-08	7.43E-11	9.31E-11	3.62E-13	2.65E+00	2.49E-11	3.17E-14	4.29E-13	5.87E-14	4.77E-12	5.08E-14	1.25E-10	2.35E-13	191.23	1.51	0.09933	0.00113	0.00082	0.00011
Conc (g/g)	K	Cl	Ca																		
	8.45E-02	7.44E-05	4.42E-03																		
Z3S	1	4.33E-08	2.16E-11	6.59E-09	1.09E-10	8.61E-11	3.63E-13	3.19E+01	4.19E-11	6.76E-14	1.78E-11	8.30E-14	5.87E-11	2.06E-13	1.23E-10	3.57E-13	128.60	2.19	1.32158	0.00725	0.03670	0.00023
J= 0.000965	2	1.58E-09	5.40E-13	1.03E-09	2.96E-12	1.14E-11	3.28E-13	4.24E+00	8.55E-13	5.30E-15	3.85E-13	1.86E-13	7.74E-12	1.42E-13	1.85E-12	9.76E-15	149.84	4.32	1.31316	0.04469	0.00599	0.00289
m= 0.00799 g	3	4.33E-09	8.70E-13	2.47E-09	6.29E-12	2.69E-11	3.88E-13	9.97E+00	3.78E-12	9.92E-15	2.31E-12	7.88E-14	5.63E-11	1.97E-13	6.24E-12	2.09E-14	153.44	2.25	4.06396	0.06044	0.01530	0.00057
	4	4.52E-09	9.30E-13	2.94E-09	5.77E-12	2.88E-11	3.88E-13	1.07E+01	5.46E-12	1.30E-14	4.11E-12	7.19E-14	1.80E-10	4.31E-13	5.34E-12	1.91E-14	169.96	2.32	12.13909	0.16667	0.02535	0.00056
	5	4.87E-09	1.05E-12	3.74E-09	4.46E-12	3.22E-11	3.89E-13	1.19E+01	6.32E-12	1.43E-14	5.20E-12	6.80E-14	2.67E-10	6.06E-13	3.86E-12	1.45E-14	192.25	2.34	16.13559	0.19898	0.02871	0.00051
	6	5.99E-09	1.29E-12	4.68E-09	5.24E-12	3.94E-11	3.89E-13	1.46E+01	7.42E-12	1.51E-14	6.11E-12	6.13E-14	2.50E-10	5.71E-13	4.46E-12	1.70E-14	196.50	1.96	12.37108	0.12574	0.02759	0.00039
	7	3.31E-09	7.50E-13	2.13E-09	4.67E-12	1.98E-11	3.88E-13	7.32E+00	3.48E-12	9.95E-15	2.49E-12	8.60E-14	1.14E-10	2.99E-13	3.99E-12	1.54E-14	179.22	3.56	11.25716	0.22395	0.02246	0.00089
	8	2.40E-09	5.70E-13	9.95E-10	5.11E-12	1.01E-11	4.48E-13	3.74E+00	2.39E-12	7.63E-15	1.38E-12	9.62E-14	6.66E-11	2.17E-13	4.72E-12	1.70E-14	164.36	7.36	12.83210	0.57222	0.02422	0.00201
	9	2.78E-09	6.60E-13	8.90E-10	6.44E-12	6.97E-12	3.88E-13	2.58E+00	2.64E-12	8.59E-15	1.35E-12	9.79E-14	6.41E-11	2.10E-13	6.36E-12	2.14E-14	210.93	11.91	17.94409	1.00647	0.03450	0.00316
	10	9.47E-09	1.98E-12	1.11E-09	2.47E-11	8.13E-12	4.18E-13	3.01E+00	6.85E-12	1.50E-14	1.47E-12	6.77E-14	4.90E-11	1.85E-13	2.80E-11	8.24E-14	224.39	12.61	11.73584	0.60729	0.03222	0.00223
Conc (g/g)	K	Cl	Ca																		
	4.99E-03	1.41E-04	4.01E-02																		

Figure 9. (Colour online) (a) Results of P-T estimate using conventional geothermobarometry with the composition of mineral pairs reported in Supplementary Material 2 (b) T-X chemical sections of the eclogite Z5S (see composition in the 'Methods' section), where $X(CO_2) = CO_2/(CO_2 + H_2O)$. The red box is a zoom of the phase assemblages in the range of 500 – 700 °C and $X(CO_2)$ between 0 and 0.1. Abbreviations for minerals and compositional end-members after Connolly (2005).

UHP metamorphism through $^{40}Ar/^{39}Ar$ on phengite and amphibole (Halama *et al.* 2014 and references therein), a long discussion about inherited and excess Ar is reported in Villa et al. (2014), who demonstrated that excess Ar was never credibly documented supported also by the absence of a grain size effect and by multichronometry (e.g. Lu-Hf and Rb-Sr). Regarding the fluid-aided retrogression, since the formation of retrograde minerals involves a recrystallization, a complete loss of Ar occurs, even at very low temperature (Maineri *et al.* 2003). Taking into account all these aspects, $^{40}Ar/^{39}Ar$ on phengite and amphibole is still a robust method for dating high-pressure rocks returning a minimum age of peak metamorphism.

Several contrasting models have been proposed to explain the formation and geodynamic evolution of the SSZ metamorphic belt (Hassanzadeh & Wernicke, 2016 and references therein; Shafaii Moghadam *et al.* 2020; Maghdour-Mashhour *et al.* 2021; Gharibnejad *et al.* 2023), mostly concerning the onset of the Neo-Tethys subduction event and the related magmatism without taking into account the occurrence of Lower Jurassic eclogites.

The MORB-like affinity of the NSMC eclogites (Davoudian et al. 2006) is testified also by data presented in this work (Table 1). However, no geochronological constraints exist on the protoliths' age. As the NSMC eclogites, as well as other units forming the SSZ metamorphic belt, show a clear Gondwanan affinity (Fergusson *et al.* 2016), they should be considered to be originally in an upper plate position during the onset of the subduction of the Neo-Tethys. A mechanism capable to drag slices of continental crust

derived from the upper plate at HP conditions should then be invoked to explain the formation of the NSMC eclogites. In the early phases of evolution of an orogen, a primary role may be played by tectonic erosion during subduction. Tectonic erosion has been widely recognized in oceanic subductions (e.g. Von Huene & Scholl, 1991; Barth & Schneiderman, 1996; Clift & Vannucchi, 2004; Clift & Hartley, 2007; Pastor-Galán *et al.* 2021) and rarely documented in continental subduction zones (e.g. Yin *et al.* 2007; Lu *et al.* 2018) or in back-arc basins (Peng *et al.* 2022). Peng *et al.* (2022) reported the occurrence of retrograde eclogites, characterized by peak metamorphic mineral assemblages with garnet, omphacite, rutile and quartz, within the Amdo microcontinent in central Tibet. These authors suggest that tectonic erosion associated with the subduction of the Amdo microcontinent beneath the Tethys Ocean accounts for the deep subduction induced by tectonic erosion of the overriding plate. Lu *et al.* (2018) also reported evidence of tectonic erosion related to continental subduction in north-western China. In this scenario, the eclogites from NSMC can thus be interpreted as lithologically heterogeneous tectonic slices derived from the upper plate, eroded and deeply buried *via* subduction channel on top of the subducting slab (Figure 10a). They subsequently underwent eclogite facies metamorphism (Figure 10b), exhumed along an exhumation channel and (re-)coupled with the crust of the overriding plate experiencing amphibolite-facies metamorphism (Figure 10c).

An additional hypothesis, that is also coherent with the upper plate derivation of the NSMC eclogites, is the subduction of tectonic slices derived from the hyperextended continental margin

Table 5. Compilation of ages of Early-Middle Jurassic magmatic activity in the SSZ

Location	Rock type	Mineral	Method	Age (Ma)	error	Reference
NW sector						
Bolban Abad	Granite and diorite	Zrn	U-Pb	146	2	Zhang et al. 2018
Bolban Abad	Granite and diorite	Zrn	U-Pb	148	2	Zhang et al. 2018
Suffi Abad	Granite and diorite	Zrn	U-Pb	156	0.6	Mahmoudi et al. 2011
Kangareh-Taghiabad	Gabbro	Zrn	U-Pb	148	4	Azizi et al. 2015a
Kangareh-Taghiabad	Gabbro	Zrn	U-Pb	158	10	Azizi et al. 2015a
Ghalaylan	Granite	Zrn	U-Pb	156	6	Azizi et al. 2015b
Ghalaylan	Granite	Zrn	U-Pb	158	2	Azizi et al. 2015b
Ghalaylan	Gabbro and monzonite	Zrn	U-Pb	149	0.2	Mahmoudi et al. 2011
Ghalaylan	Gabbro and monzonite	Zrn	U-Pb	151	0.2	Mahmoudi et al. 2011
Ghorveh	Granite and gabbro	Zrn	U-Pb	160.6	4	Yajam et al. 2015
Ghorveh	Granite and gabbro	Zrn	U-Pb	141.3	2	Yajam et al. 2015
Ghorveh	Granite and diorite	Zrn-Ttn	U-Pb/U-Th-Pb	146	2	Zhang et al. 2018
Ghorveh	Granite and diorite	Zrn-Ttn	U-Pb/U-Th-Pb	151	1	Zhang et al. 2018
Ghorveh	Porphyritic granite and diorite	Zrn	U-Pb	165	0.2	Mahmoudi et al. 2011
Ghorveh	Porphyritic granite and diorite	Zrn	U-Pb	165	0.4	Mahmoudi et al. 2011
Gorveh	Granitoid	Zrn	U-Pb	156.5	0.6	Mahmoudi et al. 2011
Gorveh	Granitoid	Zrn	U-Pb	149.3	0.2	Mahmoudi et al. 2011
Alvand, Hamedan	Granitoid	Zrn	U-Pb	165.02	0.2	Mahmoudi et al. 2011
Alvand, Hamedan	Leucogranite and granite	Zrn	U-Pb	164	2	Chiu et al. 2013
Alvand, Hamedan	Leucogranite and granite	Zrn	U-Pb	165	2	Chiu et al. 2013
Alvand, Hamedan	Gabbro	Zrn	U-Pb	166.5	1.9	Shahbazi et al. 2010
Alvand, Hamedan	Granite	Zrn	U-Pb	163.9	161.7	Shahbazi et al. 2010
Alvand, Hamedan	Leucogranite	Zrn	U-Pb	154.4	1.3	Shahbazi et al. 2010
Malayer	Granite, tonalite, granodiorite, syenogranite	Zrn	U-Pb	162	0.7	Ahadnejad et al. 2011
Malayer	Granite, tonalite, granodiorite, syenogranite	Zrn	U-Pb	187	0.3	Ahadnejad et al. 2011
Boroujerd	Quartz diorite, granodiorite	Zrn	U-Pb	170	0.2	Ahmadi Khalaji et al. 2007
Boroujerd	Quartz diorite, granodiorite	Zrn	U-Pb	172	1.5	Ahmadi Khalaji et al. 2007
Boroujerd	Granitoid	Zrn	U-Pb	169	1	Mahmoudi et al. 2011
Boroujerd	Granitoid	Zrn	U-Pb	169	172	Ahmadi Khalaji et al. 2007
Nezamabad	Monzogranite	Zrn	U-Pb	170	0.3	Mahmoudi et al. 2011
Central sector						
Astaneh	Granite	Zrn	U-Pb	168	1	Mahmoudi et al. 2011
Astaneh	Granitoid	Zrn	U-Pb	167.5	1	Mahmoudi et al. 2011
Astaneh	Granite	Zrn	U-Pb	170.7	1	Ahmadi Khalaji et al. 2007
Darjune, Azna	Gabbro	Zrn	U-Pb	170	3	Shakerardakani et al. 2015
Aligoordaz	Granite	Zrn	U-Pb	165	5	Esna-Ashari et al. 2012
Aligoordaz	Boninite-like			169.8	0.64	Esna-Ashari et al. 2016

(*Continued*)

Table 5. (*Continued*)

| Location	Rock type	Mineral	Method	Age (Ma)	error	Reference
Aligoordaz	Granite	Zrn	U-Pb	164	2.1	Chiu et al. 2013
Kolah Ghazi, S Esfahan	Granodiorite, monzogranite and syenogranite	Zrn	U-Pb	175.8	3	Bayati et al. 2017
Kolah Ghazi, S Esfahan	Granodiorite, monzogranite and syenogranite	Zrn	U-Pb	168	1	Bayati et al. 2017
Tootak, Bavanat	Aplite granite	Zrn	U-Pb	173	9	Hosseini et al. 2012
Zayanderud	Pegmatite	Zrn	U-Pb	176.5	1.65	Jamali Ashtiani et al. 2020
Quri Complex, Chah Dozdan, Chah Bazargan	Anorthosite, quartz diorite, gabbro, granite	Zrn	U-Pb	171	2	Fazlnia, 2007; Fazlnia et al. 2013
Quri Complex, Chah Dozdan, Chah Bazargan	Anorthosite, quartz diorite, gabbro, granite	Zrn	U-Pb	173	2	Fazlnia, 2007; Fazlnia et al. 2013
Quri Complex, Chah Dozdan, Chah Bazargan	Anorthosite, quartz diorite, gabbro, granite	Zrn	U-Pb	164	8	Fazlnia, 2007; Fazlnia et al. 2013
Chah Ghand	Granodiorite-gabbro	Amp	K-Ar	163	4	Sheikholeslami et al. 2008
Sargaz, NW Jiroft	Granite	Zrn	U-Pb	175.2	1.6	Chiu et al. 2013
SE sector						
Sargaz, NW Jiroft	Granite	Zrn	U-Pb	175	2	Chiu et al. 2013
Remeshk-Ramak	Granite, diorite, trondhjemite, plagiogranite	Zrn	U-Pb	170	1	Hunziker et al. 2015
Remeshk-Ramak	Granite, diorite, trondhjemite, plagiogranite	Zrn	U-Pb	176	1	Hunziker et al. 2015
Remeshk-Ramak	Granite, diorite, trondhjemite, plagiogranite	Zrn	U-Pb	153	1	Hunziker et al. 2015
Remeshk-Ramak	Granite, diorite, trondhjemite, plagiogranite	Zrn	U-Pb	166	1	Hunziker et al. 2015
Makran	Trondhjemite	Zrn	U-Pb	156.4	1.7	Hunziker et al. 2011
Makran	Trondhjemite	Zrn	U-Pb	160.5	1.4	Hunziker et al. 2011

at the ocean-continent transition (Manatschal *et al.* 2022). However, in order to lean towards this hypothesis, remnants of (meta)sedimentary sequences and fossil structures typical of rifted margins (Manatschal & Chenin, 2023) should have been recognized.

The development of a volcanic arc magmatism (Figure 10a-c) of calc-alkaline affinity either in an island arc setting (i.e. Japan-like arc) or on a continental margin (i.e. Andean-type arc) has been broadly considered as an indirect evidence that subduction of the Neo-Tethys beneath Central Iran began in the Early Jurassic (Fergusson *et al.* 2016; Hassanzadeh & Wernicke, 2016) or even at the very end of the Triassic (Berberian & King, 1981). Indeed, in addition to ubiquitous Lower Jurassic intrusive bodies (187 Ma the oldest, with a climax around 170 Ma: Figure 10e and Table 5), diffuse coeval calc-alkaline volcanism and volcaniclastic sedimentation became prevalent in the SSZ, which is the key proof of the transition from passive margin sedimentation to the growth of a magmatic arc along an active margin (Hassanzadeh & Wernicke, 2016). The occurrence of eclogites in the SSZ supports the onset of an active convergent margin on the southwestern side of Central Iran, as was already supposed in the palaeogeographic reconstructions of Berberian & King (1981). They suggested that a subduction zone was active since the Late Triassic and related to

the consumption of what they called the 'High-Zagros Alpine ocean', dividing Central Iran from Arabia. The subduction margin developed in response to the closure of the Palaeo-Tethys to the north and the accretion of Central Iran to the southern Eurasia margin. Subduction moved from the Palaeo-Tethys suture, after the Eo-Cimmerian orogenic event (Zanchi *et al.* 2009a, 2009b; Zanchetta *et al.* 2013a), to the south. Evidence of the onset of an active margin along the SSZ are the andesitic-basaltic volcanism and granitoid intrusions exposed under the Jurassic and Cretaceous sediments of the SSZ (Berberian & King, 1981).

Available data (Figure 10e and Table 5) demonstrate that the magmatic history is continuous in the time span from c. 187 Ma (Ahadnejad *et al.* 2011) to c. 141 Ma (Yajam *et al.* 2015; Figure 10e), with some variations in geochemical affinity (see Maghdour-Mashhour *et al.* 2021 for an updated review).

The beginning of subduction of the Neo-Tethys started early in the whole SSZ, from the northern to the southern sectors (Sheikholeslami, 2015), probably starting in the Late Triassic (Figure 10a). Until now, the subduction of the Neo-Tethys beneath the SSZ was traced back up to ca. 185 Ma (Davoudian *et al.* 2016) and 210-192 Ma (Wan *et al.* 2023), based on the oldest eclogite ages of the NSMC in the central sector of the SSZ. The ages from Wan *et al.* (2023) closely match our ages, but have been obtained on
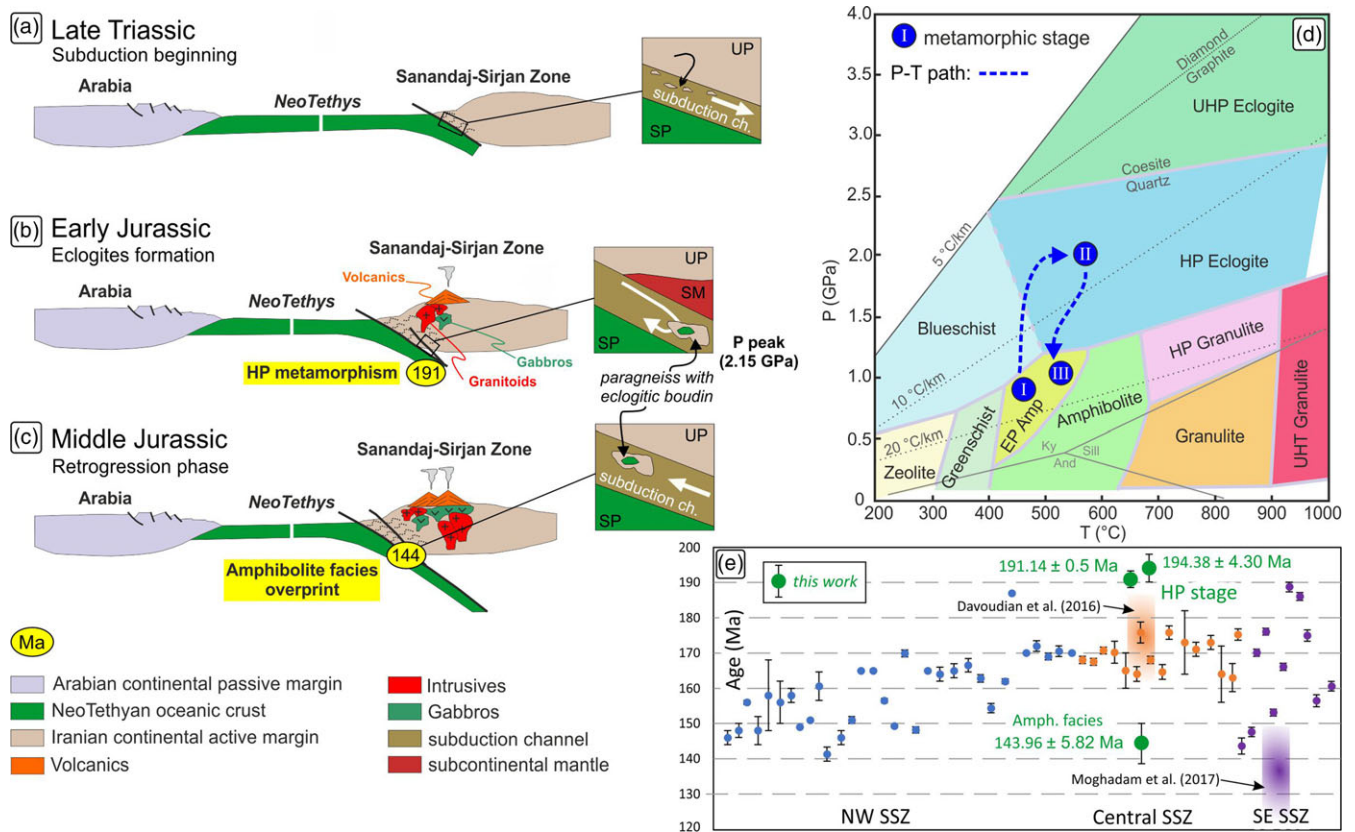
Figure 10. (Colour online) A schematic diagram showing the tectonic evolution of the SSZ from the (a) Late Triassic to the (b) Early and (c) Middle Jurassic. The white arrows in boxes (a, b, c) show the prevalent direction of materials in the subduction channel; the black arrow (a) points to the upper plate-derived rocks dragged in the subduction channel. (d) P-T path (in blue) for our studied eclogites derived from pseudosection modelling and conventional geothermobarometry. (e) Age distribution of magmatic activity in the SSZ. The orange box refers to the age of phengite in the eclogite of the NSMC from Davoudian *et al.* (2016); the violet box refers to the age of SE Zagros eclogite from Moghadam *et al.* (2017). UP: upper plate; SM: subcontinental mantle; SP: subducting plate.

rutile grains in which textural equilibrium with other syn-eclogite mineral phases (i.e. garnet and omphacite) is poorly constrained. Moreover, they consider the obtained lower intercept age as representative of peak metamorphism, even if each single age of different rutile grains displays 1σ error always larger than 30 Ma. Phengite in our samples is instead clearly related to peak metamorphism as it is in equilibrium with garnet and omphacite, as testified by microstructural fabric, constraining a minimum age for peak metamorphism. Moreover, we constrain the forward part of the P-T path, corresponding to the onset of subduction.

Magmatism started slightly earlier in the SE SSZ (Figure 10e) around 188-189 Ma (Shafaii Moghadam *et al.* 2017). From SE to NW, the onset of subduction-related magmatism becomes younger (Figure 10e), starting only at 155-160 Ma in the NW sector of the SSZ.

Our new petrological and geochronological data testify that Neo-Tethys subduction was active at least since 191-194 Ma (Figures 8a and 10b), in the earliest Jurassic, just after the end of the Eo-Cimmerian orogeny. The oldest robust geochronological data on the onset of a calc-alkaline magmatic activity in the SSZ trace back to ca. 190 Ma (Figure 10). As the onset of volcanic arc magmatism in a supra-subduction setting requires several Myrs or tens of Mrys to flare up (e.g. Stein & Stein, 1992), we should consider 191 Ma as the minimum age of subduction initiation along the SSZ. P-T estimates of the pressure peak recorded by the NSMC eclogites presented in this study, together with the ones of Davoudian *et al.* (2008), suggest a geothermal gradient < 10°C/km,

pointing to an already mature subduction zone with a cold thermal regime (Cloos, 1993).

In the Middle Jurassic (Figure 10c), the retrogression phase was going on, developing amphibolites at the expense of the eclogites. This phase is constrained at 144 Ma by $^{40}Ar/^{39}Ar$ age on amphibole (Figures 8c and 10b). The occurrence of Jurassic metamorphism in the SSZ preceding the Iran-Arabia collision is not limited to the NSMC. At its NW termination, the NSMC is in contact with the Hamadan Phyllite, a metamorphic complex mainly composed of phyllites and micaschists. The occurrence of polyphase deformation and of aluminosilicates such as andalusite, sillimanite and staurolite in several areas of the complex (Mohajjel *et al.* 2006) suggests that the Hamadan Phyllite underwent medium-grade metamorphism. Even if no direct dating is available, the intrusion ages of undeformed granitoids that cluster around 170 Ma (Ahmadi Khalaji *et al.* 2007; Mahmoudi *et al.* 2011) constrain the metamorphism in pre-Middle Jurassic times (Fergusson *et al.* 2016), so likely almost coeval with the HP event in the NSMC and subsequent amphibolite-facies retrogression.

Our new data imply that the Neo-Tethys subduction began quite before 191 Ma, therefore suggesting a subduction initiation at least 7 Myrs earlier compared to what was supposed previously (Davoudian *et al.* 2016). The age of HP eclogite facies metamorphism therefore preceded the onset of magmatism in the SSZ as should be expected for subduction-related magmatism.

Our results provide the first complete prograde-retrograde P-T-t path of eclogites in the SSZ (Figure 10d), constraining the

onset of eclogite facies metamorphism at 191 Ma (Figure 10b) and its duration up to subsequent amphibolite-facies retrogression at 144 Ma (Figure 10c). The subduction of the Neo-Tethys was accompanied by tectonic erosion from the Gondwanan overriding plate (Figure 10a), bringing the upper plate-related material to experience eclogite facies metamorphism (191 Ma, Figure 10b) and subsequent exhumation undergoing amphibolite-facies metamorphism (144 Ma, Figure 10c).

The Sinemurian age of the NSMC eclogites indicates that immediately after the end of the Eo-Cimmerian orogenesis, the subduction of the Neo-Tethys began along the southern border of the Iranian blocks, represented by the SSZ (Fergusson *et al.* 2016). The NSMC eclogites likely derived from crustal fragment of the upper plate (SSZ) that were scraped off by tectonic erosion by the subducting Neo-Tethys oceanic slab.

Evidence of a post-Cimmerian compression and plate reorganization in the Iranian geodynamic scenario is widespread. A 'subduction jump' from the Palaeo-Tethys margin to the Neo-Tethys one, i.e. the SSZ, could explain compressional deformation recorded in several parts of Central Iran in the Early to Middle Jurassic (Bagheri & Stampfli, 2008; Rahmati-Ilkhchi *et al.* 2011).

10. Conclusions

1. The eclogites of the North Shahrekord Metamorphic Complex (NSMC) derive from the Gondwanan continental crust, representing fragments of the upper plate during the Neo-Tethys subduction.

2. Three metamorphic stages and a prograde clockwise P–T trajectory are reconstructed for the NSMC eclogites: (a) an initial pre-eclogite stage preserved in garnet porphyroblasts, (b) a HP metamorphic stage at 1.90-2.15 GPa and 550-600 °C in the presence of Na-amphibole + zoisite ± carbonates and (c) a subsequent epidote-amphibolite-facies retrogression.

3. $^{40}Ar/^{39}Ar$ dating of the eclogites constrains the minimum age of peak pressure conditions at 191.14 ± 0.50 Ma, with the amphibolites-facies retrogression that was achieved at 143.96 ± 5.82 Ma. These new data indicate that the onset of Neo-Tethys subduction began at least 7 Myrs earlier than what was previously reported.

4. Due to their upper plate derivation and age of metamorphism, we propose that the NSMC eclogites of the SSZ formed in response to tectonic erosion of the Jurassic active margin of Iran, with the Neo-Tethys subduction that started just after the closure of the Palaeo-Tethys suture zone to the north in response of a wide plate reorganization in the Iranian area following the Eo-Cimmerian orogeny.

References

Agard P, Omrani J, Jolivet L and Mouthereau F (2005) Convergence history across Zagros (Iran): constraints from collisional and earlier deformation. *International Journal of Earth Sciences* **94**, 401–419. https://doi.org/10.1007/s00531-005-0481-4.

Agard P, Omrani J, Jolivet L, Whitchurch H, Vrielynck B and Spakman W (2011) Zagros orogeny: a subduction-dominated process. *Geological Magazine* **148**, 692–725.

Agard P, Yamato P, Jolivet L and Burov E (2009) Exhumation of oceanic blueschists and eclogites in subduction zones: timing and mechanisms. *Earth-Science Reviews* **92**, 53–79.

Ahadnejad V, Valizadeh MV, Deevsalar R and Rezaei-Kahkhaei M (2011) Age and geotectonic position of the Malayer granitoids: implication for plutonism in the Sanandaj-Sirjan Zone, W Iran. *Neues Jahrbuch Fur Geologie Und Palaeontologie-Abhandlungen* **261**(1), 61.

Ahmadi Khalaji A, Esmaeily D, Valizadeh MV and Rahimpour-Bonab H (2007) Petrology and geochemistry of the granitoid complex of Boroujerd, Sanandaj-Sirjan Zone, Western Iran. *Journal of Asian Earth Sciences* **29**, 859–877.

Alavi M (1994) Tectonics of Zagros Orogenic belt of Iran, new data and interpretation. *Tectonophysics* **229**, 211–238.

Alirezaei S and Hassanzadeh J (2012) Geochemistry and zircon geochronology of the Permian A-type Hasanrobat granite, Sanandaj–Sirjan belt: a new record of the Gondwana break-up in Iran. *Lithos* **151**, 122–134.

Allmendinger RW, Jordan TE, Kay SM and Isacks BL (1997) The evolution of the Altiplano^Puna plateau of the central Andes. *Annual Review of Earth and Planetary Sciences* **25**, 139–174.

Angiolini L, Zanchi A, Zanchetta S, Nicora A and Vezzoli G (2013) The Cimmerian geopuzzle: new data from South Pamir. *Terra Nova* **25**(5), 352–360.

Angiolini L, Zanchi A, Zanchetta S, Nicora A, Vuolo I, Berra F, Henderson C, Malaspina N, Rettori R, Vachard G and Vezzoli G (2015) From rift to drift in South Pamir (Tajikistan): Permian evolution of a Cimmerian terrane. *Journal of Asian Earth Sciences* **102**, 146–169.

Azizi H, Najari M, Asahara Y, Catlos EJ, Shimizu M and Yamamoto K (2015b) U-Pb zircon ages and geochemistry of Kangareh and Taghiabad mafic bodies in northern Sanandaj-Sirjan Zone, Iran: evidence for intra-oceanic arc and back-arc tectonic regime in Late Jurassic. *Tectonophysics* **660**, 47–64.

Azizi H, Zanjefili-Beiranvand M and Asahara Y (2015a) Zircon U–Pb ages and petrogenesis of a tonalite–trondhjemite–granodiorite (TTG) complex in the northern Sanandaj– Sirjan zone, northwest Iran: evidence for Late Jurassic arc–continent collision. *Lithos* **216**, 178–195.

Babaahmadi A, Mohajjel M, Eftekhari A and Davoudian AR (2012) An investigation into the fault patterns in the Chadegan region, west Iran: evidence for dextral brittle transpressional tectonics in the Sanandaj–Sirjan Zone. *Journal of Asian Earth Sciences* **43**(1), 77–88.

Bagheri S and Stampfli GM (2008) The Anarak, Jandaq and Posht-e-Badam metamorphic complexes in Central Iran: new geological data, relationships and tectonic implications. *Tectonophysics* **451**, 123–155.

Barth AP and Schneiderman JS (1996) A comparison of structures in the Andean Orogen of Northern Chile and exhumed midcrustal structures in Southern California, USA: an analogy in tectonic style? *International Geology Review* **38**, 1075–1085. https://doi.org/10.1080/00206819709465383.

Bayati M, Esmaeily D, Maghdour-Mashhour R, Li XH and Stern RJ (2017) Geochemistry and petrogenesis of Kolah-Ghazi granitoids of Iran: insights into the Jurassic Sanandaj-Sirjan magmatic arc. *Chemie Der Erde-Geochemistry* **77**, 281–302. https://doi.org/10.1016/j.chemer.2017.02.003.

Berberian F, Muir ID, Pankhurst RJ and Berberian M (1982) Late Cretaceous and early Miocene Andean-type plutonic activity in northern Makran and Central Iran. *Journal of the Geological Society London* **139**, 605–614.

Berberian M and King G (1981) Towards a paleogeography and tectonic evolution of Iran. *Canadian Journal of Earth Sciences* **8**, 210–265.

Brunet M and Cloetingh S (2003) Integrated Peri-Tethyan Basins studies (Peri-Tethys Programme). *Sedimentary Geology* **156**(1-4), 1–10. https://doi.org/10.1016/S0037-0738(02)00279-8.

Cawthorn RG and Collerson KD (1974) The recalculation of pyroxene end-member parameters and the estimation of ferrous and ferric iron content from electron microprobe analyses. *American Mineralogist* **59**(11-12), 1203–1208.

Cheng H, Liu Y, Vervoort JD and Lu H (2015) Combined U–Pb, Lu–Hf, Sm–Nd and Ar–Ar multichronometric dating on the Bailang eclogite constrains the closure timing of the Paleo-Tethys Ocean in the Lhasa terrane, Tibet. *Gondwana Research* **28**, 1482–1499.

Chiu HY, Chung SL, Zarrinkoub MH, Mohammadi SS, Khatib MM and Iizuka Y (2013) Zircon U–Pb age constraints from Iran on the magmatic evolution related to Neotethyan subduction and Zagros orogeny. *Lithos* **162**, 70–87. https://doi.org/10.1016/j.lithos.2013.01.006.

Clift P and Hartley AJ (2007) Slow rates of subduction erosion and coastal underplating along the Andean margin of Chile and Peru. *Geology* **35**, 503–506. https://doi.org/10.1130/G23584A.1.

Clift P and Vannucchi P (2004) Controls on tectonic accretion versus erosion in subduction zones: implications for the origin and recycling of the continental crust. *Reviews of Geophysics* **42**(2), RG2001.

Cloos M (1993) Lithospheric buoyancy and collisional orogenesis: Subduction of oceanic plateau, continental margins, island arcs, spreading ridges, and seamounts. *Geological Society of America Bulletin* **105**, 717–737.

Connolly JAD (2005) Computation of phase equilibria by linear programming: a tool for geodynamic modeling and its application to subduction zone decarbonation. *Earth and Planetary Science Letters* **236**, 524–541. https://doi.org/10.1016/j.epsl.2005.04.033.

Crawford A (1977) A summary of isotopic age data for Iran, Pakistan and India. *Mémoires de la Société Géologique de France* **8**, 251–260.

Davoudian A, Genser J, Neubauer F and Shabanian N (2016) ^{40}Ar/^{39}Ar mineral ages of eclogites from North Shahrekord in the Sanandaj-Sirjan Zone, Iran: implications for the tectonic evolution of Zagros orogen. *Gondwana Research* **37**, 216–240.

Davoudian AR, Genser J, Dachs E and Shabanian N (2008) Petrology of eclogites from north of Shahrekord, Sanandaj–Sirjan Zone, Iran. *Mineralogy and Petrology* **92**, 393–413.

Davoudian AR, Khalili M, Noorbehsht I, Dachs E, Genser J and Shabanian N (2006) Geochemistry of metabasites in the north of the Shahrekord, Sanandaj–Sirjan Zone, Iran. *Neues Jahrbuch für Mineralogie Abhandlungen* **182**, 291–298.

Dey A, Sen K, Sen A and Choudhary S (2023) Omphacite breakdown, symplectite formation and carbonate metasomatism in a retrograded continental eclogite: implications for the exhumation of the Tso Morari Crystalline Complex (Trans-Himalaya, NW India). *Physics and Chemistry of the Earth* **131**, 103453. https://doi.org/10.1016/j.pce.2023.103453.

Di Vincenzo G, Horton F and Palmeri R (2016) Protracted (~ 30 Ma) eclogite-facies metamorphism in northern Victoria Land (Antarctica): implications for the geodynamics of the Ross/Delamerian Orogen. *Gondwana Research* **40**, 91–106.

Di Vincenzo G and Palmeri R (2001) An ^{40}Ar–^{39}Ar investigation of high-pressure metamorphism and the retrogressive history of mafic eclogites from the Lanterman Range (Antarctica): evidence against a simple temperature control on argon transport in amphibole. *Contributions to Mineralogy and Petrology* **141**(1), 15–35.

Esna-Ashari AM, Tiepolo M and Hassanzadeh J (2016) On the occurrence and implications of Jurassic primary continental boninite-like melts in the Zagros orogen. *Lithos* **258**, 37–57.

Esna-Ashari AM, Tiepolo M, Valizadeh MV, Hassanzadeh J and Sepahi AA (2012) Geochemistry and zircon U–Pb geochronology of Aligoodarz granitoid complex, Sanandaj-Sirjan Zone, Iran. *Journal of Asian Earth Sciences* **43**, 11–22. https://doi.org/10.1016/j.jseaes.2011.09.001.

Fazlnia A (2007) Synchronous activity of two kinds of magmas, anorthosite and S-type granite, in the Chah-Dozdan intrusion, Neyriz, Iran: evidence of zircon SHRIMP UPb and monazite CHIME U-Th-total Pb dating. *Earth and Life* **2**, 24–44.

Fazlnia A, Schenk V, Appel P and Alizade A (2013) Petrology, geo- chemistry, and geochronology of the Chah-Bazargan gabbroic intrusions in the south Sanandaj-Sirjan zone, Neyriz, Iran. *International Journal of Earth Sciences* **102**, 1403–1426. https://doi.org/10.1007/s00531-013-0884-6.

Fergusson CL, Nutman AP, Mohajjel M and Bennett VC (2016) The Sanandaj–Sirjan Zone in the Neo-Tethyan suture, western Iran: Zircon U–Pb evidence of late Palaeozoic rifting of northern Gondwana and mid-Jurassic orogenesis. *Gondwana Research* **40**, 43–57. https://doi.org/10.1016/j.gr.2016.08.006.

Forneris JF and Holloway JR (2003) Phase equilibria in subducting basaltic crust: implications for H2O release from the slab. *Earth and Planetary Science Letters* **214**, 187–201.

Förster H (1974) Magmentypen und Erzlagerstätten im Iran. *Geologische Rundschau* **63**, 276–292.

Franzolin E, Schmidt MW and Poli S (2011) Ternary Ca–Fe–Mg carbonates: subsolidus phase relations at 3.5G Pa and a thermodynamic solid solution model including order/disorder. Contribution to *Mineralogy and Petrology* **161**, 213–227. https://doi.org/10.1007/s00410-010-0527-x.

Fuhrman ML and Lindsley DH (1988) Ternary-feldspar modeling and thermometry. *American Mineralogist* **73**(3-4), 201–215.

Gharibnejad P, Rosenberg CL, Agard P, Kananian A and Omrani J (2023) Structural and metamorphic evolution of the southern Sanandaj-Sirjan zone, southern Iran. *International Journal of Earth Sciences* **112**(1), 383–415.

Ghasemi A and Poor Kermani M (2009) Structure of the Soresat Metamorphic Complex, North Sanandaj–Sirjan Zone, northwest Iran. *Australian Journal of Earth Sciences* **56**, 939–949.

Ghasemi A and Talbot CJ (2006) A new tectonic scenario for the Sanandaj–Sirjan Zone (Iran). *Journal of Asian Earth Sciences* **26**, 683–693.

Giese P, Scheuber E, Schilling F, Schmitz M and Wigger P (1999) Crustal thickening processes in the Central Andes and the different natures of the Moho-discontinuity. *Journal of South American Earth Sciences* **12**, 201–220.

Giuntoli F, Lanari P and Engi M (2018) Deeply subducted continental fragments: I. Fracturing, dissolution-precipitation and diffusion processes recorded by garnet textures of the central Sesia Zone (Western Italian Alps). *Solid Earth* **9**, 167–189.

Green ECR, Holland TJB and Powell R (2007) An order-disorder model for omphacitic pyroxenes in the system jadeite-diopsidehedenbergite-acmite, with applications to eclogite rocks. *American Mineralogist* **92**, 1181–1189.

Green ECR, White RW, Diener JFA, Powell R, Holland TJB and Palin RM (2016) Activity–composition relations for the calculation of partial melting equilibria in metabasic rocks. *Journal of Metamorphic Geology* **34**, 845–869. https://doi.org/10.1111/jmg.12211.

Halama R, Konrad-Schmolke M, Sudo M, Marschall HR and Wiedenbeck M (2014) Effects of fluid–rock interaction on 40Ar/39Ar geochronology in high-pressure rocks (Sesia-Lanzo Zone, Western Alps). *Geochimica et Cosmochimica Acta* **126**, 475–494.

Hassanzadeh J, Stockli D, Horton B, Axen G, Stockli L, Grove M, Schmitt A and Walker J (2008) U-Pb zircon geochronology of late Neoproterozoic-Early Cambrian granitoids in Iran: implications for paleogeography, magmatism and exhumation history of Iranian basement. *Tectonophysics* **451**, 71–96.

Hassanzadeh J and Wernicke B (2016) The Neotethyan Sanandaj-Sirjan zone of Iran as an archetype for passive margin-arc transitions. *Tectonics* **35**, 586–621.

Hawthorne FC and Oberti R (2007) Classification of the amphiboles. *Reviews in Mineralogy and Geochemistry* **67**(1), 55–88.

Holland TJB and Powell R (1998) An internally consistent thermodynamic data set for phases of petrological interest. *Journal of Metamorphic Geology* **16**, 309–343. https://doi.org/10.1111/j.1525-1314.1998.00140.x.

Holland TJB and Powell R (2011) An improved and extended internally consistent thermodynamic dataset for phases of petrological interest, involving a new equation of state for solids. *Journal of Metamorphic Geology* **29**, 333–383.

Hosseini B, Ghorbani M, Pourmoafi SM and Ahmadi AR (2012) Identification of two different phases of metamorphosed granitoid in Kuh-Sefid Tootak anticline based on U-Pb Age dating. *Scientific Quarterly Journal of Geosciences* **21**(84), 57–66.

Huang B, Kusky TM, Johnson TE, Wilde SA, Wang L, Polat A and Fu D (2020) Paired metamorphism in the Neoarchean: a record of accretionary-to-collisional orogenesis in the North China Craton. *Earth and Planetary Science Letters* **543**, 116355.

Huang P, Wei C, Dong J and Zhang J (2023) Two-stage exhumation of high-P rocks from the Yuli Belt, Eastern Taiwan: Insights from the metamorphic evolution in subduction channels. *Lithos* **440**, 107056.

Hunziker D, Burg JP, Bouilhol P, Sergeev S and Omrani J (2011) Trace element and SHRIMP data from the Remeshk-Mokhtaramabad and Fannuj-Maskutan ophiolites: evidence for Late Jurassic subduction in N-Makran, SE Iran: EGU General Assembly. In Geophysical Research Abstracts (Vol. 13, pp. EGU2011-EGU2919).

Hunziker D, Burg JP, Bouilhol P and von Quadt A (2015) Jurassic rifting at the Eurasian Tethys margin: Geochemical and geochronological constraints from granitoids of North Makran, southeastern Iran. *Tectonics* **34**, 571–593. https://doi.org/10.1002/2014TC003768.

Hyppolito T, Cambeses A, Angiboust S, Raimondo T, García-Casco A and Juliani C (2019) Rehydration of eclogites and garnet-replacement processes during exhumation in the amphibolite facies. *Geological Society, London, Special Publications* **478**(1), 217–239.

Jamali Ashtiani R, Hassanzadeh J, Schmitt AK, Sudo M, Timmerman M, Günter C and Sobel E (2020) Geochronology and geochemistry of subducted Cadomian continental basement in central Iran: Decompressional anatexis along the Jurassic Neotethys margin. *Gondwana Research* **82**, 354–366. https://doi.org/10.1016/j.gr.2020.01.005.

Jamshidi Badr M, Collins A, Masoudi F, Cox G and Mohajjel M (2013) The U–Pb age, geochemistry and tectonic significance of granitoids in the Soursat Complex, Northwest Iran. *Turkish Journal of Earth Sciences* **22**, 1–31.

Jolivet L, Faccenna C, Goffé B, Burov E and Agard P (2003) Subduction tectonics and exhumation of high-pressure metamorphic rocks in the Mediterranean orogens. *American Journal of Science* **303**(5), 353–409.

Krogh Ravna EJ (1988) The garnet-clinopyroxene Fe-Mg geothermometer—a reinterpretation of existing experimental data. *Contributions to Mineralogy and Petrology* **99**(1), 44–48.

Krogh Ravna EJ (2000) The garnet–clinopyroxene Fe^{2+}–Mg geothermometer: an updated calibration. *Journal of Metamorphic Geology* **18**(2), 211–219.

Krogh Ravna EJ and Terry MP (2004) Geothermobarometry of UHP and HP eclogites and schists - an evaluation of equilibria among garnet-clinopyroxene-kyanite-phengite- coesite/quartz. *Journal of Metamorphic Geology* **22**(6), 579–592.

Lombardo B and Rolfo F (2000) Two contrasting eclogite types in theHimalayas: implications for the Himalayan orogeny. *Journal of Geodynamics* **30**, 37–60.

Lu Z, Zhang J and Mattinson C (2018) Tectonic erosion related to continental subduction: an example from the eastern North Qaidam Mountains, NW China. *Journal of Metamorphic Geology* **36**(5), 653–666.

Maghdour-Mashhour R, Hayes B, Pang KN, Bolhar R, Shabani AAT and Elahi-Janatmakan F (2021) Episodic subduction initiation triggered Jurassic magmatism in the Sanandaj–Sirjan zone, Iran. *Lithos* **396**, 106189.

Mahmoudi S, Corfu F, Masoudi F, Mehrabi B and Mohajjel M (2011) U-Pb dating and emplacement history of granitoid plutons in the northern Sanandaj-Sirjan Zone, Iran. *Journal of Asian Earth Sciences* **41**, 238–249.

Maineri C, Benvenuti M, Costagliola P, Dini A, Lattanzi P, Ruggieri G and Villa IM (2003) Sericitic alteration at the La Crocetta deposit (Elba Island, Italy): interplay between magmatism, tectonics and hydrothermal activity. *Mineralium Deposita* **38**, 67–86.

Malek-Mahmoudi F, Davoudian AR, Shabanian N, Azizi H, Asahara Y, Neubauer F and Dong Y (2017) Geochemistry of metabasites from the North Shahrekord metamorphic complex, Sanandaj-Sirjan Zone: Geodynamic implications for the Pan-African basement in Iran. *Precambrian Research* **293**, 56–72.

Manatschal G and Chenin P (2023) Fossil rifted margin in the Alps. *Geological Field Trips & Maps* **15**, 1–207.

Manatschal G, Chenin P, Haupert I, Masini E, Frasca G and Decarlis D (2022) The importance of Rift inheritance in Understanding the Early Collisional Evolution of the Western Alps. *Geosciences* **12**, 434.

Martin C (2019) P–T conditions of symplectite formation in the eclogites from the Western Gneiss Region (Norway). *Geological Society, London, Special Publications* **478**(1), 197–216.

Massonne HJ (2012) Formation of amphibole and clinozoisite-epidote in eclogite owing to fluid infiltration during exhumation in a subduction channel. *Journal of Petrology* **53**, 1969–1998.

Massonne HJ and Li B (2020) Zoning of eclogitic garnet cores – a key pattern demonstrating the dominance of tectonic erosion as part of the burial process of worldwide occurring eclogites. *Earth-Science Reviews* **210**, 103356. https://doi.org/10.1016/j.earscirev.2020.103356.

Mattei M, Cifelli F, Muttoni G and Rashid H (2015) Post-Cimmerian (Jurassic–Cenozoic) paleogeography and vertical axis tectonic rotations of Central Iran and the Alborz Mountains. *Journal of Asian Earth Sciences* **102**, 92–101. https://doi.org/10.1016/j.jseaes.2014.09.038.

McCall G (2002) A summary of the geology of the Iranian Makran. *Geological Society of London Special Publications* **195**(1), 147–204. https://doi.org/10.1144/GSL.SP.2002.195.01.10.

McDonough WF and Sun SS (1995) The composition of the Earth. *Chemical Geology* **120**(3–4), 223–253.

Moghadam H, Brocker M, Griffin W, Li X, Chen R and O'Reilly S (2017) Subduction, high-P metamorphism, and collision fingerprints in South Iran: constraints from zircon U-Pb and mica Rb-Sr geochronology. *Geochemistry, Geophysics, Geosystems* **18**, 306–332. https://doi.org/10.1002/2016GC006585.

Moghadam H, Khademi M, Hu Z, Stern RJ, Santos JF and Wu Y (2015) Cadomian (Ediacaran–Cambrian) arc magmatism in the ChahJam–Biarjmand metamorphic complex (Iran): magmatism along the northern active margin of Gondwana. *Gondwana Research* **27**, 439–452.

Moghadam H, Li QL, Li XH, Stern RJ, Levresse G, Santos JF, Lopez Martinez M, Ducea MN, Ghorbani G and Hassannezhad A (2020) Neo-Tethyan subduction ignited the Iran arc and backarc differently. *Journal of Geophysical Research Solid Earth* **125**(5), e2019JB018460. https://doi.org/10.1029/2019JB018460.

Mohajjel M, Bagarifar A, Moinevaziri H and Nozaem E (2006) Deformation history, micro-structure and P-T-t path in ALS-bearing schists, southeast Hamadan, Sanandaj-Sirjan zone, Iran. *Journal of the Geological Society of Iran* **1**, 11–19.

Mohajjel M and Fergusson C (2014) Jurassic to Cenozoic tectonics of the Zagros Orogen in northwestern Iran. *International Geology Review* **56**, 263–287.

Mohajjel M and Fergusson CL (2000) Dextral transpression in Late Cretaceous continental collision, Sanandaj–Sirjan zone, western Iran. *Journal of Structural Geology* **22**, 1125–1139.

Mohajjel M, Fergusson CL and Sahandi MR (2003) Cretaceous–Tertiary convergence and continental collision, Sanandaj–Sirjan Zone, western Iran. *Journal of Asian Earth Sciences* **21**, 397–412.

Montemagni C and Villa IM (2021) Geochronology of Himalayan shear zones: unravelling the timing of thrusting from structurally complex fault rocks. *Journal of the Geological Society of London* **178**, 1–13. https://doi.org/10.1144/jgs2020-235.

Montemagni C and Zanchetta S (2022) Constraining kinematic and temporal evolution of a normal-sense shear zone: insights into the Simplon Shear Zone (Western Alps). *Journal of Structural Geology* **156**, 104557. https://doi.org/10.1016/j.jsg.2022.104557.

Moritz R, Ghazban F and Singer BS (2006) Eocene gold ore formation at Muteh, Sanandaj–Sirjan tectonic zone, Western Iran: a result of late-stage extension and exhumation of metamorphic basement rocks within the Zagros Orogen. *Economic Geology* **101**, 1497–1524.

Nutman AP, Mohajjel M, Bennett VC and Fergusson CL (2014) Gondwanan Eoarchean–Neoproterozoic ancient crustal material in Iran and Turkey: Zircon U–Pb–Hf isotopic evidence. *Canadian Journal of Earth Sciences* **51**, 272–285.

O'Brien PJ and Rötzler J (2003) High-pressure granulites: formation, recovery of peak conditions and implications for tectonics. *Journal of Metamorphic Geology* **21**(1), 3–20. https://doi.org/10.1046/j.1525-1314.2003.00420.x.

Pastor-Galán D, Spencer CJ, Furukawa T and Tsujimori T (2021) Evidence for crustal removal, tectonic erosion and flare-ups from the Japanese evolving forearc sediment provenance. *Earth and Planetary Science Letters* **564**, 116893.

Pellegrino L, Malaspina N, Zanchetta S, Langone A and Tumiati S (2020) High pressure melting of eclogites and metasomatism of garnet peridotites from Monte Duria Area (Central Alps, N Italy): a proxy for melt-rock reaction during subduction. *Lithos* **358-359**, 105391. https://doi.org/10.1016/j.lithos.2020.105391.

Peng Y, Yu S, Li S, Liu Y, Santosh M, Lv P, Li Y, Li C and Liu Y (2022) Tectonic erosion and deep subduction in Central Tibet: evidence from the discovery of retrograde eclogites in the Amdo microcontinent. *Journal of Metamorphic Geology* **40**(9), 1545–1572.

Polino R, Dal Piaz GV and Gosso G (1990) An accretionary wedge model for the pre-collisional Cretaceous orogeny in the Alps. *Mémoires de la Société Géologique de France* **156**, 309–321.

Rahmati-Ilkhchi M, Faryad SW, Holub FV, Košler J and Frank W (2011) Magmatic and metamorphic evolution of the Shotur Kuh metamorphic complex (Central Iran). *International Journal of Earth Sciences* **100**, 45–62.

Ricou L (1994) Tethys reconstructed: plates, continental fragments and their boundaries since 260 Ma from Central America to Southeastern Asia. *Geodynamica Acta* **7**, 169–218.

Sadegh HR, Moeinzadeh H and Moazzen M (2020) Geochemistry and geochronology of amphibolites from the Sirjan area, Sanandaj-Sirjan zone of Iran: jurassic metamorphism prior to Arabia and Eurasia collision. *Journal of Geodynamics* **143**, 101786. https://doi.org/10.1016/j.jog.2020.101786.

Schmidt MW and Poli S (1998) Experimentally based water budgets for dehydrating slabs and consequences for arc magma generation. *Earth and Planetary Science Letters* **163**, 361–379.

Schoene B and Bowring SA (2006) U–Pb systematics of the McClure Mountain syenite: thermochronological constraints on the age of the 40Ar/39Ar standard MMhb. *Contributions to Mineralogy and Petrology* **151**, 615. https://doi.org/10.1007/s00410-006-0077-4.

Schröder JW (1944) Essai sur la structure de l'Iran. *Ecologae Geologicae Helvetiae* **37**, 37–81.

Şengör AC (1984) The cimmeride orogenic system and the tectonics of Eurasia. *Geological Society of America Special Papers* **195**, 1–74.

Şengör AC and Yilmaz Y (1981) Tethyan evolution of Turkey: a plate tectonic approach. *Tectonophysics* **75**(3-4), 181–241.

Shahbazi H, Siebel W, Pourmoafee M, Ghorbani M, Sepahi AA, Shang CK and Abedini MV (2010) Geochemistry and U–Pb zircon geochronology of the Alvand plutonic complex in Sanandaj-Sirjan Zone (Iran): new evidence for Jurassic magmatism. *Journal of Asian Earth Sciences* **39**, 668–683. https://doi.org/10.1016/j.jseaes.2010.04.014.

Shakerardakani F, Neubauer F, Masoudi F, Mehrabi B, Liu X, Dong Y, Mohajjel M, Monfaredi B and Friedel G (2015) Panafrican basement and Mesozoic gabbro in the Zagros orogenic belt in the Dorud-Azna region (NW Iran): laser-ablation ICP-MS zircon ages and geochemistry. *Tectonophysics* **647**, 146–171.

Sheikholeslami MR (2015) Deformations of Palaeozoic and Mesozoic rocks in southern Sirjan, Sanandaj–Sirjan Zone, Iran. *Journal of Asian Earth Sciences* **106**, 130–149. https://doi.org/10.1016/j.jseaes.2015.03.007.

Sheikholeslami MR, Pique A, Mobayen P, Sabzehei M, Bellon H and Emami MH (2008) Tectonometamorphic evolution of the Neyriz metamorphic complex, Quri-Kor-e-Sefid area (Sanandaj-Sirjan Zone, SW Iran). *Journal of Asian Earth Sciences* **31**, 504–521.

Spalla MI, Lardeaux JM, Dal Piaz GV, Gosso G and Messiga B (1996) Tectonic significance of Alpine eclogites. *Journal of Geodynamics* **21**(3), 257–285.

Stampfli G and Borel G (2002) A plate tectonic model for the Paleozoic and Mesozoic constrained by dynamic plate boundaries and restored synthetic oceanic isochrons. *Earth and Planetary Science Letters* **196**, 17–33.

Steiger R and Jäger E (1977) Subcommission on geochronology: convention on the use of decay constants in geo-and cosmochronology. *Earth and Planetary Science Letters* **36**, 359–362.

Stein CA and Stein S (1992) A model for the global variation in oceanic depth and heat flow with lithospheric age. *Nature* **359**, 123–129.

Stöcklin J (1968) Structural history and tectonics of Iran: a review. *American Association of Petroleum Geologists Bulletin* **52**, 12291258.

Thöni M (2006) Dating eclogite-facies metamorphism in the Eastern Alps–approaches, results, interpretations: a review. *Mineralogy and Petrology* **88**, 123–148.

Vannucchi P, Remitti F and Bettelli G (2008) Geological record of fluid flow and seismogenesis along an erosive subducting plate boundary. *Nature* **451**(7179), 699–703.

Villa IM, Bucher S, Bousquet R, Kleinhanns IC and Schmid SM (2014) Dating polygenetic metamorphic assemblages along a transect across the Western Alps. *Journal of Petrology* **55**, 803–830. https://doi.org/10.1093/petrology/egu007.

Von Huene R and Scholl DW (1991) Observations at convergent margins concerning sediment subduction, subduction erosion, and the growth of continental crust. *Reviews of Geophysics* **29**, 279–316. https://doi.org/10.1029/91RG00969.

Wan B, Chu Y, Chen L, Zhang Z, Ao S and Talebian M (2023) When and why the Neo-Tethyan subduction initiated along the Eurasian margin: a case study from a Jurassic eclogite in southern Iran. *Compressional Tectonics: Plate Convergence to Mountain Building* **1**, Chapter 9. https://doi.org/10.1002/9781119773856.ch9.

Warren C, Smye A, Kelley S and Sherlock S (2012) Using white mica ^{40}Ar/^{39}Ar data as a tracer for fluid flow and permeability under high-P conditions: Tauern Window, Eastern Alps. *Journal of Metamorphic Geology* **30**, 63–80.

Wei CJ and Clarke GL (2011) Calculated phase equilibria for MORB compositions: a reappraisal of the metamorphic evolution of lawsonite eclogite. *Journal of Metamorphic Geology* **29**(9), 939–952.

White R, Powell R, Holland TJB, Johnson T and Green E (2014) New mineral activity-composition relations for thermodynamic calculations in metapelitic systems. *Journal of Metamorphic Geology* **32**(3), 261–286.

White RW, Powell R and Clarke GL (2002) The interpretation of reaction textures in Fe-rich metapelitic granulites of the Musgrave Block, central Australia: constraints from mineral equilibria calculations in the system $K_2O–FeO–MgO–Al_2O_3–SiO_2–H_2O–TiO_2–Fe_2O_3$. *Journal of Metamorphic Geology* **20**, 41–55.

Whitney DL and Evans BW (2010) Abbreviations for names of rock-forming minerals. *American Mineralogist* **95**(1), 185–187.

Wilke FDH, O'Brien PJ, Gerdes A, Timmerman MJ, Sudo M and Khan MA (2010) The multistage exhumation history of the Kaghan Valley UHP series, NW Himalaya, Pakistan from U-Pb and ^{40}Ar/^{39}Ar ages. *European Journal of Mineralogy* **22**, 703–719.

Wilmsen M, Fursich FT and Taheri J (2009) The Shemshak Group (Lower–Middle Jurassic) of the Binalud Mountains, NE Iran: stratigraphy, depositional environments and geodynamic implications. *Geological Society of London, Special Publications* **312**, 175–188.

Yajam S, Montero P, Scarrow JH, Ghalamghash J, Razavi SMH and Bea F (2015) The spatial and compositional evolution of the Late Jurassic Ghorveh-Dehgolan plutons of the Zagros Orogen, Iran: SHRIMP zircon U-Pb dating and Sr and Nd isotope evidence. *Geologica Acta: An International Earth Science Journal* **13**, 25–43.

Yin A, Manning CE, Lovera O, Menold CA, Chen X and Gehrels GE (2007) Early Palaeozoic tectonic and thermomechanical evolution of ultrahigh-pressure (UHP) metamorphic rocks in the Northern Tibetan Plateau, Northwest China. *International Geology Review* **49**, 681–716. https://doi.org/10.2747/0020-6814.49.8.681.

Zanchetta S, Berra F, Zanchi A, Bergomi M, Caridroit M, Nicora M and Heidarzadeh G (2013a) The record of the Late Palaeozoic active margin of the Palaeotethys in NE Iran: Constraints on the Cimmerian orogeny. *Gondwana Research* **24**, 1237–1266. https://doi.org/10.1016/j.gr.2013.02.013.

Zanchetta S, Poli S, Rubatto D, Zanchi A and Bove GM (2013b) Evidence of deep subduction of Austroalpine crust (Texel Complex, NE Italy). *Rendiconti dell'Accademia Nazionale dei Lincei* **24**, 163–176.

Zanchetta S, Worthington J, Angiolini L, Leven EJ, Villa IM and Zanchi A (2018) The Bashgumbaz Complex (Tajikistan): Arc obduction in the Cimmerian orogeny of the Pamir. *Gondwana Research* **57**, 170–190.

Zanchi A, Malaspina N, Zanchetta S, Berra F, Benciolini L, Bergomi M, Cavallo A, Javadi HR and Kouhpeyma M (2015) The Cimmerian accretionary wedge of Anarak, Central Iran. *Journal of Asian Earth Sciences* **102**, 45–72.

Zanchi A, Zanchetta S, Balini M and Ghassemi MR (2016) Oblique convergence during the Cimmerian collision: evidence from the Triassic Aghdarband Basin, NE Iran. *Gondwana Research* **38**, 149–170. https://doi.org/10.1016/j.gr.2015.11.008.

Zanchi A, Zanchetta S, Berra F, Mattei M, Garzanti E and Molyneux S (2009a) The Eo-Cimmerian (Late? Triassic) orogeny in north Iran. *Geological Society of London Special Publications* **312**, 31–55.

Zanchi A, Zanchetta S, Berra F, Mattei M, Javadi HR and Montemagni C (2021) Cenozoic Dextral Shearing Along the Arusan Sector of the Great Kavir–Doruneh Fault System (Central Iran). *Tectonics* **40**(11), e2021TC006766.

Zanchi A, Zanchetta S, Garzanti E, Balini M, Berra F, Mattei M and Muttoni G (2009b) The Cimmerian evolution of the Nakhlak-Anarak area Central Iran and its bearing for the reconstruction of the history of the Eurasian margin. *Geological Society of London Special Publications* **312**(1), 261–286.

Zhang Z, Xiao W, Ji W, Majidifard MR, Rezaeian M, Talebian M, Xiang D, Chen L, Wan B, Ao S and Esmaeili R (2018) Geochemistry, zircon U-Pb and Hf isotope for granitoids, NW Sanandaj-Sirjan zone, Iran: implications for Mesozoic-Cenozoic episodic magmatism during Neo-Tethyan lithospheric subduction. *Gondwana Research* **62**, 227–245.